Synthesis and Characterization of CuFe₂O₄ / rGO Composite

By

Aamina Batool

School of Chemical and Materials Engineering (SCME)

National University of Sciences and Technology (NUST)

2017

Synthesis and Characterization of Copper Ferrite / rGO Nanocomposite

Name: Aamina Batool

Reg. No: NUST201362362MSCME67913F

This thesis is submitted as a partial fulfillment of the requirements for

the degree of

MS in Nanoscience and Engineering

Supervisor Name: Dr. Iftikhar Hussain Gul

School of Chemical and Materials Engineering (SCME)

National University of Sciences and Technology (NUST)

H-12 Islamabad, Pakistan

June, 2017

Certificate

This is to certify that work in this thesis has been carried out by **Ms. Aamina Batool** and completed under my supervision in Thermal Transport Laboratory, School of Chemical and Materials Engineering, National University of Sciences and

Technology, H-12, Islamabad, Pakistan.

Supervisor**:** _____

Prof. Dr. Iftikhar Hussain Gul

Thermal Transport Laboratory

Material Engineering Department

National University of Sciences and Technology,

 Islamabad

Submitted through

Principal/Dean,

School of Chemical and Materials Engineering Department

National University of Sciences and Technology, Islamabad

Dedication

I dedicate this thesis to my mother

Saima Nasim

Acknowledgements:

In the name of Allah, the most Beneficent and the most Merciful. First and foremost, I thank Allah, for being my guide and helper throughout the degree tenure.

Next I wish to express gratitude to the guides on Earth; Principal of SCME and HOD Materials Engineering for providing me with all the necessary facilities for the research. My supervisor, who has been immensely kind in his guidance. I am more indebted to him than can be put in words. Without his cooperation and effort, this research would never have been completed.

I thank my lab fellows for facilitating me and offering sincere advice always. The lab attendants, and all other department staff who have been greatly honest with their work. My classmates for great companionship throughout the research phase.

Finally, I owe thanks to my family members. My father, for his benevolence and for his undying care. My mother, for being the most loving mother in the world, despite great hardships. And my siblings for all their love, support and cheerful company.

I owe immense gratitude to the people mentioned above, for it is their guidance, prayers and belief that has kept me going. May Allah shower His blessings on them and keep them under His shade. Ameen.

Warm Regards,

Aamina Batool.

Abstract:

A facile one-step method of thermochemical reaction was approached for the synthesis of $CuFe_2O_4$/rGO hybrid composite. The study design inculcated an increment of GO wt. % (0%, 5%, 10% and 15%) in starting precursors whereby GO was simultaneously reduced to rGO during the reaction. The composites were characterized by X-Ray Diffraction (XRD), Scanning Electron Microscope (SEM), Fourier Transform Infrared Spectroscopy (FT-IR) and Impedance Analyzer and Galvanostatic Charge-Discharge testing. The XRD patterns confirmed the reduction of GO and formation of $CuFe_2O_4$/rGO composite. Moreover, the crystallite size of the $CuFe_2O_4$/rGO composite was obtained in the range of 48 ± 6 nm, The FTIR results showed two major vibrational bands, confirming the spinel structure formation. The SEM images showed embedding of $CuFe_2O_4$ nanoparticles on rGO sheets. The dielectric properties were highly enhanced with increasing wt. % of GO in the $CuFe_2O_4$. Pure $CuFe_2O_4$ exhibited a dielectric constant of 3.57×10^4 at 100 Hz that was enhanced massively to 1.27×10^5 for 15 wt. % of GO. Also, the dielectric loss values depicted an increase from the 3.24×10^5 for pure $CuFe_2O_4$ to 1.42×10^6 for 15 wt. % of GO, making this nanohybrid composite a potential candidate for supercapacitor applications. The charge storage capacity, cyclic stability and rate capability were also enhanced with increasing wt. % of GO. The specific capacity for 15 wt. % of GO was 1190 mAh g^{-1} for 1st and 845 mAh g^{-1} for 25th cycle, comparable to pure $CuFe_2O_4$ values of 900 mAh g^{-1} for 1st and 625 mAh g^{-1} for 25th cycle. Hence a substantial enhancement of electrochemical properties was depicted that projects the composite as a useful candidate for application as an electrode material for lithium-ion batteries.

Table of Contents

Chapter 1: Introduction

Chapter 2: Theoretical Review

Chapter 3: Characterization Techniques

Chapter 4: Results and Discussion:

List of Figures

Chapter 1: Introduction

Chapter 2: Theoretical Review

Chapter 3: Characterization Techniques

Chapter 4: Results and Discussion

List of Tables

Chapter 1: Introduction

Chapter 4: Results and Discussion

Chapter 1

Introduction

1.1 Nanomaterials and Nanotechnology

Nanotechnology is a field that exclusively finds niche in the groundbreaking rejoinder, "plenty of room (space) at the bottom", as stated by the revolutionary physicist R. Feynman [49]. This 21st century technology ascribes to the synthesis and exploitation of ultra-fine particles, and employing their novel properties to a plethora of dynamic fields. Scientifically speaking, the research pertains to synthesis and engineering at nano-scale regime and subsequent investigation into material properties and phenomena. The particles existing at nanometric dimensions display superlative chemical, physical, electrical, optical and magnetic characteristics in contrast to their bulk sized cousins. The fundamental motivation for fabrication of materials include the ever-soaring demand of high density storage media at smaller size dimension. [46]

The idea of a nanoscale energy storage system is not nascent and has been around for decades. The technology emerged in 1980's and was an outcome of 'convergence' research, a principle that inculcates disciplinary approaches from sciences previously considered distinct and separate.

This collaboration of experimental advances such as the development of scanning tunneling microscope in 1981 and subsequent discovery of fullerenes in 1985 brought a revolution in the convergence research [47]. It led to an elucidation of the conceptual goals of nano-research. The merging of processes and devices into unified whole, creating opportunities for technological advancement became one of the defining facets of nanotechnology. The commercial applications of nanotechnology commenced in early 2000's and thrives till date [48]. The transformative applications envisioned by nanotechnology continue to be the main focus of scientists and engineers.

1.2 Historical Background of Ferrites:

Ferrites of the semiconductor family, are mixed metallic oxides that exhibit high resistivity. Ferrites are found naturally occurring in nature as magnetite, and displays poor magnetic properties. It was nearing the end of World War 1, when Japanese scientists Kato and Takei [24], Kawai [25] and from Netherlands, Snoek [26] started exploiting ferromagnetic materials. Later in 1943 the first framework for understanding ferrimagnetism was presented by Neel [27]. The magnetic sub-lattices and the underlying spin to spin interactions were explained for the first time. Eventually, the first modern ferrite was formulated in 1946 [28]. The first ferrite permeability tensor allowed for understanding ferrites at microwave frequency, and was developed in 1949 by Polder [29]. The applicability took root, and the first ferrite microwave generator was developed by Hogan [30]. After this period, ferrites were used extensively in commercial applications such as transformer and television tubes. In recent years, the demand for ferrites has increased owing to usage in biomedical industry, automotive industry, power supplies and circuits.

1.3 Magnetic Materials:

All materials are categorized as magnetic or non-magnetic, so are nanomaterials.

a) **Non-Magnetic Materials:**

Materials that lack in magnetic domains are characterized as non-magnetic. Plastic, wood and glass are inherently non-magnetic.

b) **Magnetic Materials:**

Materials that internalize magnetic domains are magnetic materials. These materials do not extensively exist by volume. They have significant applications in electronics engineering systems and are categorized into soft and hard magnetic materials.

1.3.1 Soft Magnetic Materials:

Soft magnetic materials are easily attracted to a permanent magnet. When placed under the effect of external magnetic field, the materials that are easily magnetized but retain the magnetism for a short time span are known as soft magnetic materials. These materials do not generate a large magnetic field [63]. They find applications in memory storage devices, electronic components, transformers, generators, motors and microwave devices. Examples are nickel, cobalt and iron [64].

1.3.2 Hard Magnetic Materials:

Generally used as permanent magnets, the hard magnetic materials can produce a strong magnetic field to the outside. When placed under the effect of external field, the materials that are not easily magnetized but retain the magnetism for a considerably long time are denoted as hard magnetic materials. They find applications in servo motors, quality audio headphones, MRI body scanners, floppy discs [65].

1.4 Classification of Magnetic Materials:

The magnetic properties of a material are dependent on various internal and external factors. The magnetic susceptibility and saturation magnetization are dependent on atomic or molecular structure as well as magnetic moments of atoms. The external factors, like temperature also play a role in determining magnetization. The atomic magnetic moment value is given by Bohr magnetron as 9.27×10^{-24} Am^2. An electron spins around its axis, and orbits the nucleus, giving rise to an intrinsic magnetic field. Electrons usually form a pair of opposing spin alignment (up and down) and hence, balance and cancel out each other's effect. The magnetic field exists in atoms with an odd number of electrons where all spins are not cancelled and balanced. These atoms form tiny magnets, and the regions within the structure where these tiny magnets align are denoted as domains.

The magnetic materials are categorized into following classification based on their properties like saturation magnetization, permeability, susceptibility and magnetic behavior.

1. Diamagnetic materials
2. Paramagnetic materials
3. Ferromagnetic/Ferrimagnetic materials
4. Anti-ferromagnetic materials
5. Superparamagnetic materials

1.4.1 Diamagnetic Materials:

Those materials where the net magnetic moment amounts to zero owing to balancing and cancelling of spins are known as diamagnetic materials. These materials contain an even number of electrons and hence no unbalanced spins. They also have zero magnetic susceptibility. Popular examples include plastic, wood, bismuth, gold and copper.
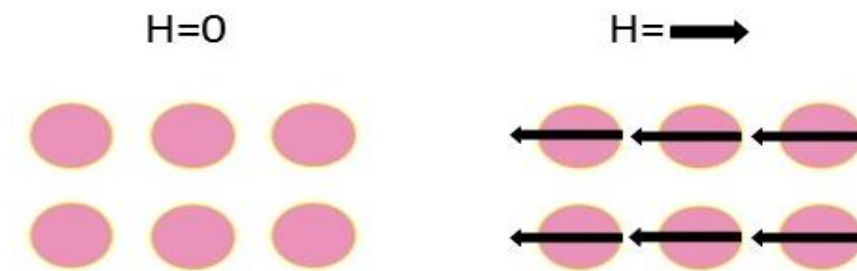
Figure 1.1: A Diamagnetic Material

1.4.2 Paramagnetic Materials

The materials that contain atoms and molecules with permanent magnetic moment are known as paramagnetic materials. These atoms contain unbalanced and incomplete cancellation of spins that are aligned by an external magnetic field. They have a positive but low magnetic susceptibility, which is temperature dependent, hence they are not very

strongly attracted to external fields, owing to lesser number of unbalanced tiny magnets. Well known examples include tungsten, cesium and sodium.
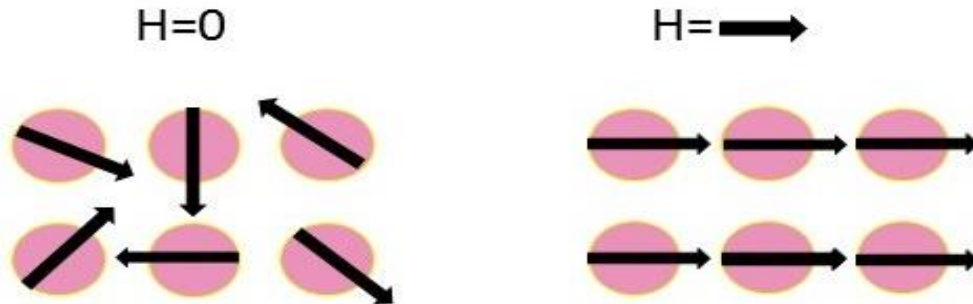
Figure 1.2: A Paramagnetic Material

1.4.3 Ferromagnetic Materials

According to ordering of spins, the diamagnetic and paramagnetic types pertain to disordered magnets while the ferromagnetic materials are the ordered magnets. These materials exhibit remarkable affinity towards external fields, retaining magnetic moment long after the removal of extraneous magnetic field. The structure contains unpaired electrons that maintain a net magnetic moment and the strong interaction between domains tend to keep remaining aligned after the removal of external field. Examples include, cobalt, ferrites, garnets, nickel and iron etc. They show spontaneous magnetization at low temperatures and a large value of positive magnetic susceptibility and exist in nature as insulators of electricity [66].
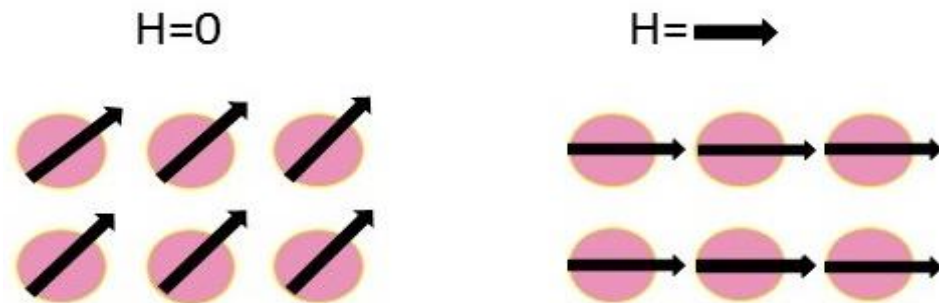
Figure 1.3: A Ferromagnetic Material

1.4.4 Anti-ferromagnetic Materials:

Neel predicted the presence of the cooperative magnetic phenomenon of anti-ferromagnetism. These materials encompass of electrons with a spin, opposing the spin of neighboring electrons, hence the dipole moments are dependent on these spin directions. The electrons in the two interpenetrating equivalent sub-lattices balance, and cancel out the net dipole moment. The magnetization albeit, has a small positive value. Above a certain temperature known as Neel's temperature, these materials start exhibiting the characteristics of paramagnetic materials. When the extraneous magnetic field is removed, there is no magnetization [67]. Examples include, nickel oxide, chromium, iron manganese alloys.
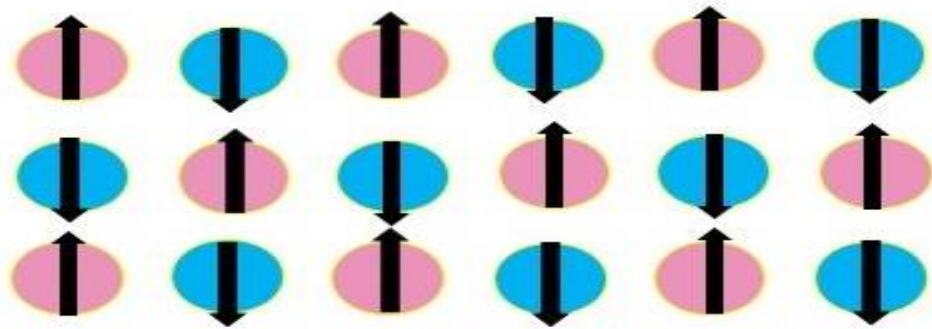
Figure 1.4: An Antiferromagnetic Material

1.4.5 Ferrimagnetic Materials

The phenomenon in which the electrons residing in the sub-lattices are still oppositely directed, but the magnitude is not equivalent. Since the magnetic moment of an atom residing in sub-lattice A is greater than sub-lattice B, there will no balancing or cancelling of dipoles. It is due to this reason that these substances show net magnetization after the removal of extraneous field of magnetism, much like ferromagnets. And just like ferromagnets, they turn into paramagnetic materials above Curie temperature. These materials show zero magnetic susceptibility, no eddy currents, and are non-conducting [66]. Examples include MnO, oxides and ionic compounds.
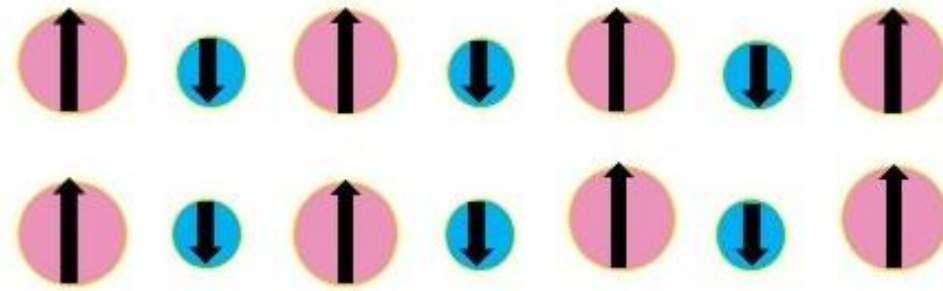
Figure 1.5: A Ferrimagnetic Material

1.4.6 Superparamagnetic Materials

The materials that exhibit the properties of a paramagnetic materials below Curie temperature or Neel temperature and lose their magnetic properties. These materials contains atoms in neighboring sub-lattices augmenting the magnetic moments of neighboring atoms. Hence large internal magnetic fields are created due to the presence of coupling forces [68].

1.5 Ferrites:

Ferrites pertain to the classification of ferrimagnetic materials, which implies that they are attracted towards magnet, are insulators electrically and are mainly composed of iron oxide. The naturally occurring ferrous ferrite is magnetite, given by formula Fe (Fe_2O_4) or Fe_2O_3. These materials find applications in permanent magnets and transformer cores. They are extensively used in high frequency application owing to the high electrical resistivity of ferrites. They have low eddy currents and hysteresis losses. Ferrites can be categorized into two structural symmetries on the basis of charge of metallic ion, and mass. These are known as cubic and hexagonal symmetries [69]. On the basis of hysteresis losses, they can be classified into soft ferrites and hard ferrites.

1.5.1 Soft Ferrites:

Soft ferrites pertain to the type of ferrites than exhibit magnetism when exposed to a magnetic field, and unlike their hard counterparts, allow no recollection of magnetism long after removal of extraneous field of magnetism. Consequently, a low externally applied magnetic field results in large changes in magnetic flux density. The ease of magnetization and demagnetization stems from low coercivity and high resistivity. Low coercivity implies the direction of magnetization can be easily reversed without dissipation of energy (heat) to hysteresis loss. High resistivity hinders loss of energy by preventing eddy currents. Soft ferrites have an extensive applicability in power supplies as cores for inductors and RF transformers [1]

Examples: $SrFe_{12}O_{19}$ ($SrO.6Fe_2O_3$**,** Ni-$ZnFe_2O_4$, $NiFe_2O$, $BaFe_{12}O_{19}$ ($BaO·6Fe_2O_3$), NiFe, FeSi, FeCo**,** $CoFe_2O_4$ ($CoO·Fe_2O_3$), Metallic Ni, Fe, Garnets etc.

Applications:

1. Magnetic deflection structures
2. Rotating Transformers
3. Recording Heads
4. Transducers/Inducers
5. Shield Beds and Chokes

Table 1.1 Comparison of Properties of Soft and Hard Ferrites

Properties	Soft Ferrites	Hard Ferrite
Hysteresis Energy Loss	Low	Very High
Hysteresis Loop Area	Long and Thin	Wide
Saturation Magnetization	Low	High
Coercive Field	Low (A few A/m)	High (12.5 to 250 A/m)
Eddy Current Loss	More	Less
Permeability Value	Higher	Lower
Susceptibility Value	Greater	Smaller

Magnostatic Energy	Small	High
Structure of pure ferrite	Hexagonal (subject to presence of impurities)	Cubic (subject to presence of impurities)
Electrical Resistivity	High	Low
Magneto-crystalline Anisotropy	Low	High
Curie Temperature	High	Low

1.5.2 Hard ferrites:

Hard ferrites pertain to the type of ferrite that retain magnetism when removed from a magnetic field. The magnetic hardness originates from the crystalline anisotropy of particles, and are characterized by large coercivity and high remanence after magnetization. Hence, do not allow for easy magnetization and demagnetization. The amount of residual magnetism held by these ferrites can be fairly large after the removal of external field. The high coercivity ensures the existence of these ferrites as permanent magnets that can store stronger magnetic fields than iron. They conduct magnetic flux. The density of these magnets is 5gm/cm3 and they are cost effective. The maximum magnetic field of these ferrites is 0.35 tesla. [2]

Examples: Rare Earth Metal Alloys, Cobalt ferrite: $CoFe_2O_4$ ($CoO \cdot Fe_2O_3$), Strontium ferrite: $SrFe_{12}O_{19}$ ($SRO \cdot 6Fe_2O_3$, Mn_a $Zn_{(1-a)}$ Fe_2O_4), AlNiCo, Barium ferrite: $BaFe_{12}O_{19}$ ($BaO \cdot 6Fe_2O_3$)

Applications:

1. Small Electric Motors
2. Magnetic Detectors
3. Loudspeakers
4. Voltage Regulator
5. Permanent Magnet [11]

1.6 Classification of ferrites:

The term ferrite is attributed to magnetic oxides encompassing iron oxide as main constituent. The crystallographic structure is classified into three dissimilar type viz. hexagonal ferrites, garnet ferrites and spinel ferrites [23]. The ferrite substances exhibit different soft and hard magnetic places.

1.6.1 Hexagonal ferrite:

The ferrites that crystallize in hexagonal structure contain the general formula $MFe_{12}O_{19}$ and have gained significant technological advancement after their identification in 1952 [21]. The 'M' in the formula pertains to a divalent ion of large ionic radius, like strontium (Sr), lead (Pb) or barium (Ba). The charge compensation is maintained through presence of one ion per formula unit of Fe^{2+}. The unit cell is hexagonal, contains oxygen lattice in FCC alignment. It is quite alike the spinel configuration owing to closely aligned oxygen structure, although in contrast, the layers include metal ions. These metal ions exhibit the same ionic radii as oxygen ions. Consequently, the structure contains metals at three loci, namely tetrahedral, octahedral and trigonal pyramid. A series of hexagonal layers of oxygen align perpendicular to the (111) direction [8]. One unit contains two molecules of $MeFe_{12}O_{19}$. The basic structure is complex hexagonal comprising a unique c axis or vertical axis. These ferrites maintain a high magnetocrystalline anisotropy with the c axis, which is easy axis of magnetization. This high anisotropy is ascribed to the Fe^{3+} ions located at the trigonal bi-pyramidal site. This makes them ideal candidates for permanent magnetic materials that exhibit high coercivity. The hexagonal ferrites are classified as "hard" ferrites as the direction of magnetization does not change to another axis with ease. In comparison with garnet counterparts, the hexagonal ferrites accept larger ions through replacing oxygen ions by metal ions [20]

1.6.2 Garnet ferrites:

Natural garnet comprises of a cubic structure of FCC type and is given by the general formula $B_3Fe_5O_{12}$ where B_3 comprises of rare earth metal ions (Gd, Sm, Eu, Er, Tb, Dy, Lu, Ho, or Lu) or Yttrium Iron. The first silicon-free garnet was prepared in 1951 by Yoder and Keith through substitution of mineral garnet $Mn_3Al_2Si_3O_{12}$ by YIII+AlIII from MnII+SiIV [21]. Hence the first prepared garnet was Yttrium Iron Garnet (YIC). The unit cell comprises of 160 atoms within 8 molecules of $B_3Fe_5O_{12}$, forming a cubic edge length of 12.5 Å. The crystal lattice of garnet includes three interstitial sites denoted as octahedral (A), tetrahedral (D) and Dodecahedral (C) sites. The octahedral sites are inhabited by sixteen Fe^3 ions, twenty four Fe^3 ions are located at tetrahedral loci. The Fe^3 ions are situated at tetrahedral loci and the octahedral coordination is present in ratio 3:2. The magnetic interactions between ions of octahedral and tetragonal sites are strong, owing to the large angle between the two iron atoms through the oxygen anion. On the other hand, the trivalent metal ions occupy the dodecahedral sites (C) sites where one ion is surrounded by eight oxygen ions. The bond angle between eight metal ions and the trivalent atoms is almost 900. The entire distribution can consequently be observed as [Me_3] C [Fe_2] A [Fe_3] D [O_{12}]. It is interesting to note that the net ferrimagnetism is thus, a complex result of the anti-parallel spin alignment within the 3 described sites. A unit cell of garnet exhibits edge length of about 12.5 Å and pertains to the magnetically 'hard' ferrites.

1.6.3 Ortho-ferrites

Ortho-ferrites are ferrites, comprised of an orthorhombic unit cell, are represented by the formula $MeFeO_3$, where Me denotes a large trivalent ion. They exhibit weak ferromagnetism and crystallize as distorted perovskite structure. The magnetic properties are attributed to presence of small canting within the two anti-ferromagnetically coupled lattices. The alignment allows for a canting angle of the order 10^{-2} rad and gives rise to a net ferromagnetic moment [19]. At room temperature, the direction of spin orientation of Fe ion in $ErFeO_3$ [22] has been found to exist parallel to (100) axis. Upon lowering the temperature, the spin axis rotates as well. When the cation is a rare earth ion, the spin moment gets ordered at a lower Neel temperature.

1.6.4 Spinel Ferrite

The general formula for a spinel ferrites is MFe_2O_4. In M in this formula is given by a divalent positive ion that is metallic (for example cobalt or zinc). Moreover, the spinel structure only forms when the ion radius of M is less than or equal to 1 Å. In the instances where it exceeds 1 Å, the Coulomb force proves inadequate to ensure stability of the crystal [3]. Hence, ions like Mn^{2+} with ionic radius 0.91 Å participates in forming spinel structure and Ca^{2+} with ionic radius of 1.06 Å does not form a spinel structure The oldest spinel structure was determined by Brages and Nishikawa in 1915 and belonged to $MgAl_2O$ [6].

Spinel lattice comprises of a cubic unit structure (FCC), containing eight divalent and sixteen trivalent ions disseminated over eight tetrahedral and sixteen octahedral interstices. To understand the structure better, the unit cell can be subdivided into eight octants. The octants can be divided into two types. The octants that share the faces are dissimilar whilst the octants occupying edges are similar. Every octant comprises of four oxygen ions lying body diagonal and these ions lie at the distance of one-fourth of body diagonal at opposing corners of the octant. The ion locus on the lattice depends on temperature, lattice size and orbital preference specific co-ordinates. It is important to understand that the radii of ion pertaining to oxygen are greater in size compared to ions of metals. Hence, this configuration is a closest possible fit of the oxygen ion with metallic ions residing at the interstices. [5].The divalent ions occupy larger space than trivalent ions. The electron orbit of trivalent ions are contracted due to greater electronic attraction. So the larger divalent ions reside in the larger octahedral sites whilst the contracted trivalent ions occupy the smaller tetrahedral sites.

Table 1.2 Spin Ferrite Ionic Radii [75]

Ion	Ionic Radius
Fe^{2+}	0.83
Fe^{3+}	0.67
Co^{2+}	0.82
Zn^{2+}	0.74
Mn^{3+}	0.70

The lattice contains 96 interstices, 72 of which are empty and 24 are occupied by a cation. The cationic distribution maintains charge neutrality in the following sites:

1. Tetrahedral (A) sites

2. Octahedral (B) sites.

1.6.4.1 Tetrahedral Sites: The unit cell of ferrite contains 64 tetrahedral sites, out of which 8 are occupied by cations for charge neutrality. This configuration contains metallic cation at the center with four anions locating at the corners. Three out of four anions are in a plane whilst the fourth one resides at the top [4].
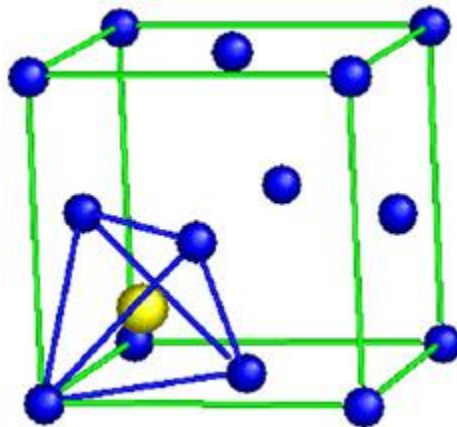
Figure 1.6: Tetrahedral Sites in Spinel Structure [76]

1.6.4.2 Octahedral Sites: The unit cell contains 32 octahedral sites, out of which, 16 are occupied by cations for charge neutrality. This configuration contains metallic cation at the epicenter of the cubic structure, where six negative ions flank the corners. Four of the stated negative ions are in a plane and the two anions left are located overhead and beneath the epicenter of structure plane.
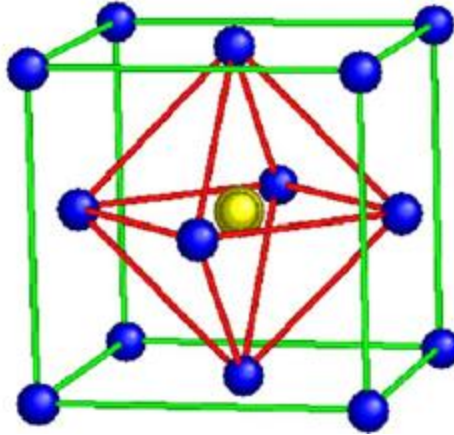
Figure 1.7: Octahedral Sites in Spinel Structure [76]

1.7 Cationic Distribution in Spinel Ferrites:

Barth and Ponjak classified spinel ferrites through cationic arrangement at the tetrahedral interstices and octahedral loci into following types:

a). Normal spinel ferrite

b). Inverse spinel ferrite

c). Mixed/Random spinel ferrite
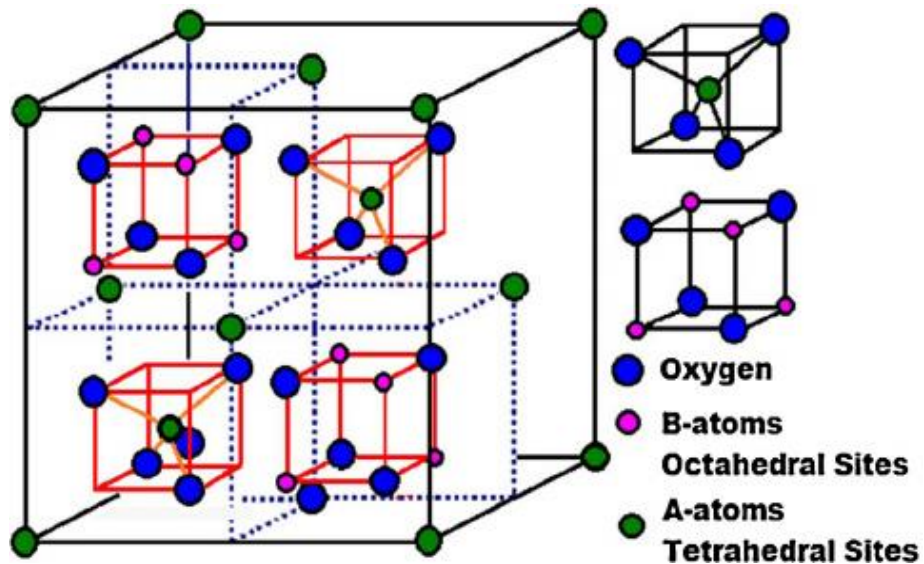
Figure 1.8: Unit structure of Spinel Ferrites [76]

1.7.1 Normal spinel ferrite:

These spinel ferrites contain divalent cations M^{2+} at tetrahedral interstices (denoted by A) only. Moreover the trivalent cations occupy octahedral interstices (denoted by B). Limited or zero interaction between tetrahedral loci and octahedral loci is seen because tetrahedral A sites do not contain magnetic ions. The alternate planes of B sub-lattices are magnetized in opposing directions. Consequently, normal spinel ferrites are non-magnetic.

Normal spinel ferrite is represented by $[M^{2+}]$ A $[Fe^{3+}]$ BO_4^{2-}. The 'M' in the formula represents divalent metal ions and 'Fe^{3+}' represents trivalent ions

Examples: $ZnFe_2O_4$, $CdFe_2O_4$

1.7.2 Inverse spinel ferrite:

The trivalent metal ion arrangement in inverse spinel caused Verwey and Heilmann to term them 'inverse' or contrast to normal spinels in 1947. As observed, the divalent positive ions M^{2+} reside at octahedral loci (B) and the trivalent positive ions Fe^{3+} are dispersed through tetrahedral loci and octahedral loci. The arrangement is such that one trivalent ferric cation occupies the tetrahedral site whilst the remaining trivalent ions and divalent ions reside at octahedral sites. As the direction of moment on A sites is opposite to B sites, the spin moments of the trivalent cations cancel out each other. The spin moments of divalent cations are aligned though and contribute to a net magnetic moment. Consequently, inverse spinel ferrites are ferrimagnetic.

Inverse spinel ferrites are represented by $[Fe^{3+}]$ A $[M_2+Fe^{3+}]$ BO_4^{2-}. The 'M' in the formula represents divalent metal ions and 'Fe^{3+}' represents trivalent ions [9].

Examples: $CuFe_2O_4$, $CoFe_2O_4$, $MnFe_2O_4$, $NiFe_2O_4$

1.7.3 Random/Mixed Spinel Ferrite:

The trivalent positive ions (cations) given by Fe^{3+} as well as the divalent ions (cations) represented by M^{2+} are disseminated at the octahedral (B) and tetrahedral (A) sites [10]. The factors that impact the dissemination of cations over these interstices are Ionic radii, physico-chemical conditions of preparation, electrostatic energy of lattice [7], sintering process and the electronic configuration of cations.

Mixed/Random spinel ferrite is represented by $[M_\delta^{2+} Me_{1-\delta}^{3+}]$ A $[M_{1-\delta}^{2+} Me_{1+\delta}^{3+}]$ BO_4 where δ is inversion parameter depicting the normalcy of metal ion. When $\delta = 1$, the structure forms a complete normal spinel ferrite, at $\delta = 0$ a complete inverse spinel is formed. The δ lies amid the given values in cases of random/mixed spinel ferrites, forming complete mixed/random spinel ferrite at $\delta = 1/3$ [12-18].

Examples: $MnFe_2O_4$ $CuFe_2O_4$, $MgFe_2O_4$

1.8 Copper Ferrite:

Ferrites having general formula of MFe_2O_4 (where M=Zn, Mn, Cu, Mg, Co etc.) are immensely investigated for their high specific capacity, short path for charge diffusion and penetration, larger surface compared to volume, better electronic conductivity and variable oxidation state. Among ferrites, $CuFe_2O_4$ nanoparticles are potentially ideal target due to its large values of capacity reported in theory, cost effectivity, high abundance, environmental safety and easy separation. Copper ferrite has a simple, inverse cubic spinel structure [53]. The thermal treatment and synthesis conditions determine the atomic arrangement in the copper ferrite products. It has a magnetic moment, amounting to 3 and has increased saturation magnetization. The lucrative properties offered by copper ferrites is their robust mechanical stability, cost effectiveness, easy availability of raw materials, suitability in high frequency applications, great magnetic properties and high coercivity. These materials also infer remarkable electrical stability, time stability and temperature stability, have great dielectric properties and exhibit promise in microwave frequency applications [55]. The disadvantages of these nanoparticles are poor cycling performance and irreversible capacity loss followed with the long life due to the poor electronic

conductivity and large volume variation. These performances can be modified by the addition of conductive fillers like graphene, reduced graphene oxide (rGO), carbon nanotubes (CNTs), carbon Nano platelets (CNPs) or carbon nanofibers (CNFs). In this regard, rGO as conductive fillers have been studied by various researchers [54].
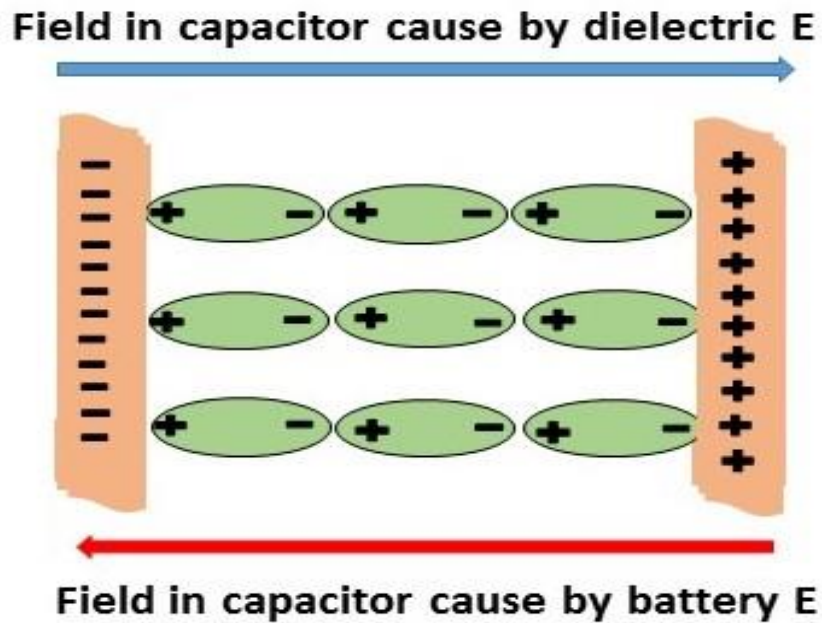
Figure: 1.9: The Dielectric Dipole Orientation in a Capacitor

1.8.1 Applications of Ferrites:

The ferrite based nanomaterials are currently exploited in a plethora of fascinating applications. Some applications are stated below:

1. Nanoparticles are used in pollution control. These devices scavenge pollutants from water streams using ferrite nanoparticles [59]. These precursor particles precipitate with pollutant materials like mercury and produce safe products that can be easily removed magnetically.

2. Nanoparticulated ferrites in a polymer matrix exhibit great mechanical strength, and thus are used in heavy vehicles in replacement of conventional heavy metals.

These composites are resistant to corrosion and allow for better fuel efficiency and higher vehicle speed.

3. Nanoferrites have applications in entertainment sector as television and radio circuits. Also, in power supply applications as microprocessor and computers [60]. In all electronic equipment, nanoparticles are used as a noise filter within power lines [62].

4. Nanoferrites have applications in the defense fields, as paints containing ferrites can absorb radar and render a submarine or aircraft invisible.

5. Ferrite nanoparticles have great applications in biological fields as drug delivery vehicle, water disinfectant, biosensor [57], biomedicine [58], cancer imaging and therapy, pesticide delivery, agriculture and cancer imaging [56].

1.9 Introduction to GO:

Graphene oxide is a chemically altered and greatly oxidized form of graphene. It is one of the analogues or derivatives of graphite flakes. Graphene oxide has a morphology of a single atom thick graphene sheet with functional groups of carboxylic acid, hydroxyl groups and epoxide exist in a plane. The carboxylic charges residing on the periphery impart a stability effect to the structure by adding negative charges to the surface. The hydroxyl and epoxide groups, in contrast, reside at the basal planes of structure. These groups impart surface reactivity and weak interactions with other functionalities. The basal planes also encompass unaltered, free π electrons. These electrons impart hydrophobicity to the basal planes, and enable the attachment of hydrophobic moieties to the thin graphene oxide sheet. Thus, owing to the existence of hydrophobic and hydrophilic functionalities, the structure exhibits an amphiphilic sheet-like character. The properties of graphene oxide make it a favored choice for nanomaterial composite synthesis. The practical advantages of utilizing graphene oxide include cost-effectiveness, scalability of graphene and easy accessibility of the structure. It has applications in a plethora of fields including energetics, biological applications, materials engineering systems and electrochemical sensing. The fascinating properties and ubiquitous use of graphene in research has initiated the beginning of a novel class of materials known as GOBM (graphene oxide based materials).

Graphene oxide has demonstrated incredible promise in the fields of energy materials and biological engineering systems [71].

1.10 Synthesis of Graphene oxide and its derivatives:

The graphite flakes comprise of polycrystalline particles, generally obtained from natural sources or produced synthetically. Graphene oxide is essentially a derivative of graphite flakes. These graphite flakes, as means of a natural source of graphite are preferred as they have internalized defects within the aromatic structure. These localized defects provide seeding points, and facilitate the chemical reaction processes involving graphene. Graphene and the corresponding derivatives are synthesized by two ways; the top down method/approach and the bottom-up method/approach. The bottom-up methodology includes chemical vapor deposition (CVD), that leads to deposition of a single layer of GO on the selected substrate at target site. The top-down approach is directed at cleaving of the multiple layers within graphite into single layers employing mechanical, physical exfoliation and chemical methods. The top down approach is the preferred method of graphene derivative synthesis. The chemical exfoliation method, pertaining to top down approach is generally carried out by Hummer's, Brodie and Staudenmaier method. Hummer's method utilizes the oxidization effect of potassium permanganate ($KMNO_4$) and sulfuric acid (H_2SO_4). Under the oxidizing influence of strong acids such as HNO_3 and H_2SO_4, the graphene flakes are transformed into graphite salts. These salts are the precursors to the subsequent GO preparation through oxidation [72].

Hummer's method is the most commonly employed method for GO synthesis. Among the most remarkable advantages of the Hummer's method, is the economy of temperature and time. The Hummer's process leads to production of graphene oxide within two hours and requiring only 45 degree temperature. Among the disadvantages or downsides of using Hummer's method is release of toxic gasses such as NO_2 and ClO_2. It is for this reason that Hummer's method is modified to inculcate environmentally friendly reagents.

Modified Hummer's method generally employs the protocol changes designed by Kovtyukhova et al and improvements developed by Marcano et al. The modified version of Hummer's method makes use of H_2SO_4, $KMnO_4$ and $NaNO_3$ as oxidizing agents. The

initial disadvantage of release of toxic gases is curbed through this modification and it produces large amount of hydrophilic GO. The exfoliation approaches are exploited to include gentle steps and reagents that lead to a cost-effective, low waste, and low toxicity green synthesis of GO [71].

1.11 Modifications Imparted on GO

The properties of GO can be remarkably altered by introducing surface modifications. These altered properties are vital to various biomedical applications. The surface modification facilitated by GO allows for conjugation of various moieties to the surface that render biologically significant properties.

The surface modifications of GO are carried out by two major approaches. One is the covalently imparted modification and the other one is the non-covalently adjoined modification. The covalent modification pose the disadvantage of destroying some already present conjugating entities, hence compromising and suppressing the properties of the final product. The non-covalent modifications, by contrast, inculcate methodologies such as electrostatic and hydrophobic interaction, π-π stacking as well as Van der Waal's forces. These superior facets of non-covalent modifications help in preservation of structure of GO and its naturally imparted properties [73-74].

1.11.1 Covalent Modification

Graphene's crystal lattice naturally contains defects and reactive oxygen species. These sites act as a reactive position for covalent linking of conjugates. The covalent modifications are carried out through various reactions that include, condensation, electrophilic addition, nucleophilic substitution and addition. During the nucleophilic substitution reactions, the main reactive sites are posed by epoxy groups present on GO. The amino-functional groups interact with GO by attack on the epoxy groups by the lone-pairs of amino group. This is a fine example of nucleophilic substitution. The nucleophilic substitution reactions impart a major advantage of ability to be carried out at room temperature and within an aqueous environment. Hence, they are the most promising and lucrative method for the commercialized, large scale modification of GO [74].

1.11.2 Non-covalent Modification

The non-covalent modification are a preferred method for the modification of the sp^2 carbon materials. Examples of such materials are graphene and CNTs. These modifications include reactions like coordinate bonding, hydrogen bonding, electrostatic and π- π interactions. The non-covalent modifications in graphene encompass absorption of polymer, surfactants and small biomolecules and other small molecules. Instances of small molecules include peptides, DNA and porphyrins. Non covalent interactions were first reported by Stankovich et al. They accounted the synthesis of graphitic nano-platelets using poly (sodium 4-styrenesulphonate) or PSS.

Instances of other functionalities using non-covalent interaction include Tween (polyoxyethylene sorbitan laurate), BSA (bovine serum albumin), Pluronic F127, CHA (cholesteryl hyaluronic acid) and PEI (polyethylenimine). These hybrid composites are demonstrating promising use in drug delivery, photo thermal therapy, and lithium ion battery [73].
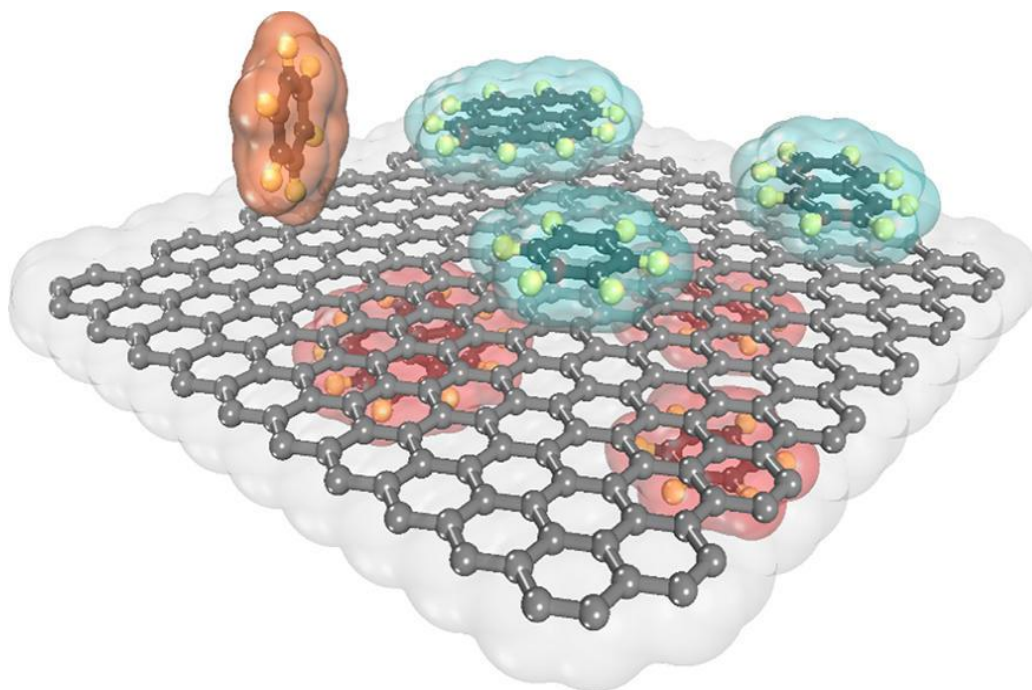
Figure 1.10: Conceptualized π−π interactions & or of C−H-π with RGO [77]

1.12 Graphene as Electrode Material:

Since a few years, graphene has been demonstrating inspiring advantages as electrode materials of a Li ion battery. It offers great benefits in a standalone fashion as well [31]. The high conductivity rendered by graphene in a system, allows fast motion of electrons to and from the intercalation sites of the active material [32]. Graphene used as an electrode removes the need of a binding polymer, as it acts as a binder itself [33].

The electronic transport efficiency of graphene is particularly enhanced when a composite when nanoparticles is formed, owing to the close physical interaction between rGO sheets and nanomaterials. The nanoparticles experience enlargement and shrinkage during the intercalation and abstraction process of electrodes. These changes are effectively absorbed by the mechanical robustness rendered by graphene [32]. When the contraction and expansion of nanomaterials are not accommodated by the system, it causes reduced performance, mechanical breakdown as well as loss of intimate contact between conductive carbon black and employed composite of electrode.

Graphene has been proven to demonstrate better cyclic stability as well as storage capacity as compared to conventional graphite electrode [34-36]. This is attributed to greater surface area of graphene, in contrast to graphite. The chemical reduction of graphene allows for better charge/discharge rates and capacity in electrodes. In lithium ion batteries, reduced graphene exhibits armchair edge effects as well as zig zag electronic effects [37-40]. This is caused by the creases, zig zags and armchair features of rGO, and causes remarkable Li+ intercalation [41]. These effects countered the drawback of single layer graphene where Li+ do not undergo considerable intercalation owing to the Li+ repulsion [42]. The structural defects stemming from the reduction process of graphene to rGO allow for great inhibition of Li+ repulsion, causing effective immersion into most non conducting host sites that are neutral electrically.

The application of reduced graphene as Li ion battery cathode, resides in its nascent stage, and its potential is yet to be exploited completely. The viable Li ion battery cathodes still suffer limitations pertaining to cathode ordering, phase transitions, stability, excessive reactivity between solvent and electrolyte (reaching beyond SEI, occurring at highly-

oxidizing electrode surface) and low conductivity [43]. Employing reduced graphene caters to the limitations of structural stability, low conductivity and reactions between electrolyte/solvent. Moreover the binding effects rendered by graphene allows for greater benefits than were initially pre-requisite.

The reduced graphene-nanocomposite synthesized by an optimal method, causes the nanomaterials of very small size to be completely embedded into the graphene sheets, providing synergistic benefits [44]. These composites are expected to retain the mechanical robustness during the cyclic intercalation and extraction processes, owing to high surface to volume ratios [45].

The metal oxide nanoparticles reach a step further in the synergistic benefits by dictating the interlayer spacing between graphene sheets. This provides a prospect to optimize the material for enhanced performance in a Li+ ion battery during diffusion and intercalation processes.

1.13 Copper Ferrite/Go Composite: Rationale behind Composite Formation

Nanotechnology can viewed exclusively as the technology pertaining to 21st Century that ascribes to preparation of ultra-fine materials at the nano-scale regime, and exploiting their potential in a plethora of dynamic fields. Modern day energy needs are every increasing, thus accentuating the need for alternative energy storage sources.

The remarkable electrical and morphological properties of graphene oxide have led to extensive engineering of these oxides for possible device applications. The chemical structure, ease of synthesis, amphiphilic sheet-like character, scalability and low cost of graphene oxide has led to investigations of these oxides in fields of energetics, biological applications and electrochemical sensing [61].

The 'convergence' research, inculcating research and disciplinary approaches from sciences previously considered distinct and separate. The technological collaboration leads to merging of processes and devices into a unified whole, creating revolutionary

opportunities for scientific and technological advancement [52]. The revolutionary convergence research has advanced across various knowledge bases, coordinating nanotechnology, microbiology to computer science to engineering design. The convergence between biological and physical sciences has been accentuated by world leaders like Barack Obama in 2000 [50]. It entails a capitalizing of ambitious and strategic coordinative research for advancement in industry, government, academia and healthcare. The challenges of the future can be met utilizing this approach, leading to alternate energy sources, economic and wth and better healthcare [51].

Researchers are attempting to integrate two or more materials with complementing properties to produce a composite with enhanced required properties and lower efficiency limitations. The spinel ferrites are great candidates for development of composite materials with aims of better electrochemical and electronic properties. They possess fascinating intrinsic functionalities. The interplay of orbital ordering, spin and charge along with influence of lattice effects allows for formation of a desirable system for application oriented research. They have a general formula MFe_2O_4 (where M is Zn, Ni, Mn, Mg and Cu). Copper ferrites are extensively studied due to their intrinsic electric and magnetic properties. Their functionalities of low eddy current losses for high frequency wave formation, permeability and resistivity allow for a rewarding playground for technical applications. The possibility of modifying the properties of these ferrites and potentially generating novel efficiencies is a lucrative perspective. Several methods are employed for synthesis of these ferrites, including thermal decomposition, sol gel method, thermolysis, co-precipitation techniques, hydrothermal synthesis, microwave synthesis, gel assisted hydrothermal synthesis, and wet chemical routes.

The alternative energy demands have seen considerable increment in the last few years, attributed to the rapid depletion of traditional of fossil bases and rapid energy consumption by a growing population. A major limitation to the development of alternative energy remains its dependence on renewable energy reserves (solar, wind and tidal energy) as well as the demand and supply gap. In this perspective, the lithium ion storage systems have attracted extensive attention due to lucrative functionalities like cyclic stability, rate capability, high power density and remarkable reversibility. These functionalities allow for

its applicability in energy storage systems like laptops, cell phones and hybrid electric vehicles (HEVs). In light of these factors, the need of the hour remains the enhancement of dielectric properties and electrochemical characteristics of these batteries.

1.14 Objectives of Study:

1. Synthesis of copper ferrite nanoparticulated oxides through a cost effective and simple method.
2. Synthesis of graphene oxides utilizing one-step facile method
3. To analyze the influence of the hybrid composite on the electronic, electrochemical and morphological properties.
4. To analyze effect of increasing weight percentage of graphene oxide within the composite.

Chapter 2

Theoretical Review

2.1 Approaches to Nanoparticle Synthesis:

The patterning and preparatory methods of nanostructured species are founded in well-designed techniques. These techniques and their preceding modifications can be broadly placed into "the top down" and "bottom up" approaches.

2.1.1 Bottom-Up Methodology:

In the Bottom-up methology, the short-range fundamental forces guide the process of assembly of atoms and molecules as starting factors, employing the principle of chemical recognition. Thus the chemical assembly of atoms or molecules using thorough understanding of short-range intra and intermolecular forces of attraction at play, like electrostatic forces, Van der Waals forces constitutes the bottom up approach. This approach allows for control of morphological control and a certain order of chemical 'versatility'. Examples of this approach include colloidal dispersion, chemical vapor growth and self-assembly.

2.1.2 Top-Down Methodology:

The top down methodology flips the bottom up approach by employing large entities in bulk and break them down into smaller ones, forgoing atomic-level control. Using microfabrication methods and moving towards a nanometer size-regime, a stark abrupt change in the characteristics like optical, physical, electrical, thermal and mechanical properties is observed. The materials exhibit different properties at nano-regime, compared to their macro-counterparts. These changes are attributed to increase in surface to volume ratio, lowering of grain size, increment in grain boundary junctions,

pores and interfaces. Also, defects are generated in constituting atoms and lattices through this approach. Some opaque materials become transparent at nanoscale (for example: copper). Gold is insoluble at macro-size but becomes soluble at nano-scale. Changes in reactivity and ion transfer are observed as well. The popular examples of this technique include surface modification, lithography, vapor treatment and etching and patterning techniques like photolithography and ink-jet printing.

2.2 Synthesis Techniques of Nanoparticles:

Synthesis of nanoparticles through different methods, allows for tweaking of electric, magnetic and morphological functionalities. Some of the widely used methods are stated below:

- Chemical Co-Precipitation Method
- Hydrothermal Method
- Micro-Emulsion Method
- Gas Condensation Process
- Sol-gel Technique
- Combustion Flame Synthesis
- Sono Chemical Method
- Poly Vinyl Alcohol (PVA) Evaporation Method
- Solvothermal Synthesis

Sol-Gel Method allows for complete homogeneity and is cost effective. Using this method, the product formation at low temperatures can be controlled. The particles obtained through this method find applications in optics and electronics. Poly Vinyl Alcohol (PVA) evaporation method is cost effective as PVA is cheap and readily available. This method produces uniformly sized particles. Gas condensation process utilizes inert gas at high pressure in a vacuum chamber. This method is not suitable for the production of spherical particles.

Large scale production of nanomaterials is achieved through flame processes. It has the advantage of being a one-step process with no machinery required to be mobile. The important drawback of this method includes the lack of control over the nanoparticle functionalities [78]. The micro-emulsion technique, reverse micelle is formed through dissolution of surfactant in organic solvent. The surfactant molecules are surrounded by water molecules, effectively forming a micro-scale reactor for nanoparticle synthesis. Precipitation step allows for production of fine ferrite nanoparticles in these micro-sized water-in-oil reactors [79]. The sono chemical method is carried out under ultrasonic waves, where starting materials react with each other. The major advantage of this method is the size reduction and low size distribution. The morphological properties can be controlled and uniformity of dissolution is achieved [80]. The hydrothermal/solvothermal methods are simple and effective processes that allow for a remarkable control over particle morphology by control over recrystallization. Various nanocrystals, nanorods, hollow spheres, urchin-like crystals can be synthesized through this cost effective and easy method.

The current research employed co-precipitation methods for the formation of copper ferrites, hence the process is explained in detail below.

2.3 Chemical Co-Precipitation Method:

The chemical co-precipitation method has become the choice method for production of nanoferrites as it allows for synthesis in a short duration. The known disadvantages of this method include the emission of fumes as well as the lack of control over the particle size beyond a known range. Simply put, the reactants are dissolved in water in the ratios determined by the protocol. The solution pH is maintained by addition of sodium hydroxide. The initial precipitation process leads to nucleation of particles but it is rapidly replaced by thermodynamically stable and desirable growth. In order for the co-precipitation to occur in the medium, the nucleation rate should exceed the growth rate [81].

The method is significant chiefly because it is cost effective and easy and the resultant product is fairly homogenous and pure. The crystallinity of the nanoparticles is influenced by impurities and rate of reaction of the employed synthesizing method. The nanoparticle shape, size and morphology is affected by super saturation affects, growth rate and nucleation. Particle size reduction is observed in cases where super saturation is high. The reaction parameters such as Rate of reaction and transport of chemicals is dependent upon concentration of starting reactants. The degree of precipitation is dependent on factors like temperature and pH.
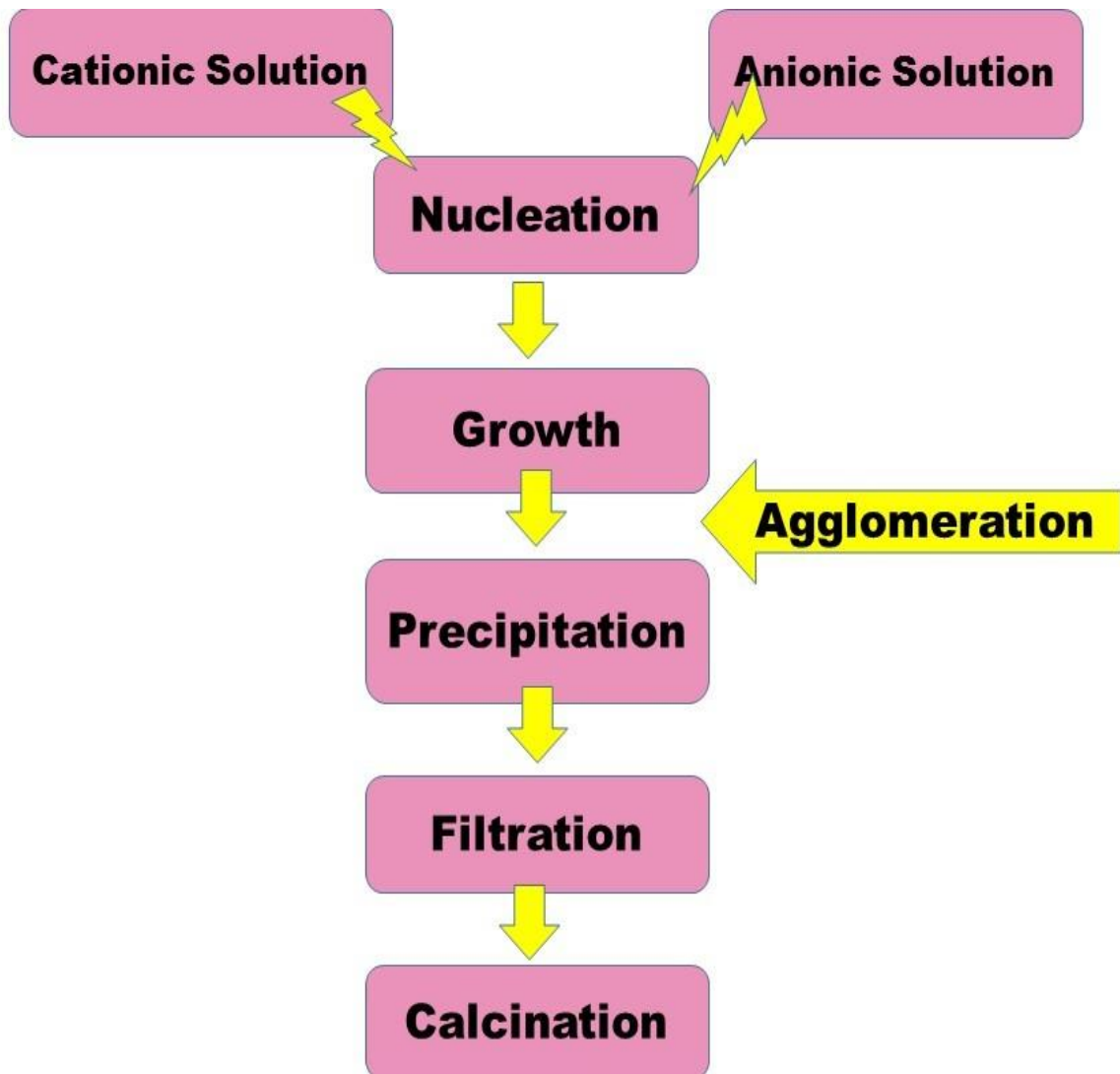
Figure 2.1: Reaction Steps of Co-Precipitation

The co-precipitation process is carried out in two major steps that are denoted as:

a) **Co-precipitation step.**

b) **Ferritisation step.**

2.3.1 Co-precipitation step:

During this stage, the colloidal particles pertaining to the solid hydroxides of metals are obtained through co-precipitation of metal cations in alkaline medium. For the case of copper ferrite, the reaction takes the following steps

$$Cu\ (NO_3)_2.\ 6H_2O\ +\ Fe\ (NO_3)_2.\ 9H_2O + NaOH$$

$$\Downarrow$$

$$Cu\ (OH)_2.\ Fe\ (OH)_3 + NaNO_3$$
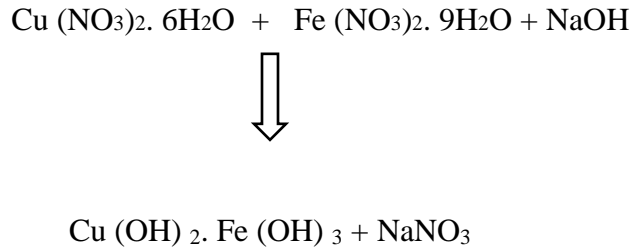
2.3.2 Ferritisation step:

This step encompasses the subjection of the product to heating in the solution that is alkaline for precipitation. This allows for conversion of the metal hydroxide solution to the copper ferrites. The hydroxide used in the first step is heated further to convert it into ferrite of copper

$$Cu\ (OH)_2.\ Fe\ (OH)_3 +\ NaNO_3$$

$$\Downarrow$$

$$Cu\ (Fe_2O_4)_2.\ nH_2O + (4\text{-}n)\ H_2O + NaNO_3$$
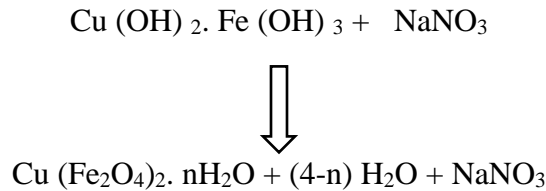
The product resulting from this step contains a certain level of associated water molecules even after it is subjected to several hours of heating in an alkaline solution. The morphological characteristics like shape, size and precipitation of the nanoparticles produced, depend on a number of factors. The impurities are removed thoroughly through

multiple washing steps utilizing deionized water. The washing steps turn the pH to 7 (or neutral) and remove impurities that are mainly ionic in nature.

2.4 Synthesis Parameters and Their Influence:

The process of co-precipitation is governed and influenced by the following factors:

1. Reagents Mixing Rate
2. Role of Anions/Cations
3. Influence of Temperature
4. Effect of pH
5. Influence of Concentration of Reagents
6. Duration of Heating after Co-precipitation

2.4.1 Reagents Mixing Rate

This parameter carries out a paramount part in determination of size of the resultant particles. The co-precipitation step encompasses of 2 sub-steps. The nucleation step, forming the centers of crystallization and the subsequent growth step, allowing growth of nanoparticles. The relative rate of the sub-processes acts as a determining factor of size and polydispersity of product. Small particle sizes originate when nucleation rate is higher than growth rate. Larger particle sizes emerge from a growth rate that surpasses nucleation rate. A higher nucleation rate compared to the growth rate is desired to attain good mixing of reagents. The polydispersed colloids are obtained from concurrent creation of nuclei and subsequent growth of previously synthesized particles. The colloid formation, less disseminated in size is attained when the nucleation rate is considerably higher than the growth rate. This setup involves vigorous mixing and rapid addition of reagents in the reaction. Small and homogenous particles are obtained through higher nucleation rate.

Slow addition of reagents in the reaction mixture, allows for construction of bigger nuclei than rapid addition does. Thus, ferrite particles of smaller size of lesser dispersion and chemical homogeneity is obtained through fast mixing of reagents [82].

2.4.2 Role of Anions/Cations:

The type of anions employed in the co-precipitation process influences the properties of obtained product differently. Different metals impart different corresponding characteristics, hence influencing properties present in the concluding nanoparticle sample. Thus, nature of the employed cation/anion is taken into consideration. The metals salts allow for better properties, hence metal salts of sulfates, nitrates and chlorides are used.

2.4.3 Influence of Temperature:

An increment in the temperate within the range of 20° to 100^oC is a reliable way of greatly accelerating the formation of ferrites. Different metals have different activation energy values for the nanoferrite formation, given the temperature is same for all. When the reactant mixture is heated, the activation energy is provided to metals. The formation of copper ferrites commences at low temperature and proceeds very robustly. The present study kept the reaction temperature at 85^oC.

2.4.4 Influence of PH:

PH has a vital influence in controlling particle shape and particle size of nanoferrites. The lower values of pH allow for no significant or considerable growth rate. Growth rate is high at high pH values and low at low pH values. A higher growth rate reduces the time required for product formation. For the synthesis of copper ferrite, the product yield is augmented when pH is increased from 6.8 to 8.6. At higher pH values still (12.5-14) the time for formation of copper ferrites is considerably reduced and a high growth is attained.

2.4.5 Duration of Heating after Co-Precipitation:

The process of co-precipitation is confined within a concentrated system. The ending step of co-precipitation is the annealing process and that allows for distinct phase

formation. The smaller size and distinct phase is obtained when the amount and duration of heat are kept optimal. In the present study the heating after co-precipitation was kept at 30 minutes after formation.

2.4.6 Influence of Concentration of Reagents:

The concentration of 0.00, 0.25, 0.50, 0.75 and 1.00 mol/l is usually employed for the synthesis of ferrite particles. At this concentration, non-viscous primary suspension of particles occurs, that brings advantageous effects to mixing of reacting volume. At higher concentration, the suspension becomes viscous and the stirring process is hindered [82].

2.5 Apparatus Specification:

Following apparatus was utilized for the synthesis of copper ferrite nanoparticles:

❖ Stirring Machine
❖ Digital Balance
❖ Hydraulic Press
❖ pH Meter
❖ Centrifugal Machine
❖ Ceramics Crucibles
❖ Mortar and Pestle
❖ Furnace

2.6 Advantages of Co-Precipitation Method:

The protocol of co-precipitation, presents the following advantages over other available methods:

❖ Cost-effective method
❖ Less time-consuming
❖ Simple method

❖ Allows for control over particle formation

❖ Allows for control over particle size

❖ Allows for control over particle shape

❖ Homogeneity of the yield product

❖ Small size of product compared to other methods [81]

2.7 GRAPHENE OXIDE: Synthesis of reduced Graphene Oxide:

Graphene oxide was obtained, that was prepared through Improved Hummer's Method. The rationale behind the selection of this method was that it is easy to carry out, cost effective and environmentally/biologically friendly.

The protocol encompassed mixing of 320 ml of sulfuric acid (H_2SO_4) with 80 ml of phosphoric acid (H_3PO_4) and stirring for 10 minutes at room temperature (4:1; 320:80 ml). To this concoction, the flakes of graphite weighing 3.0g was added slowly, while consistent stirring. This mixture was sonicated for an hour. After sonication, 18 gram of potassium permanganate was very carefully poured into the solution, to prevent production of excessive heat [84].

The oxidation process was allowed to proceed by leaving the solution at room temperature for 72 hours. The solution at the commencement of oxidation was dark green in color. After the process, it turned dark brown which served as a confirmation step for occurrence of oxidation. The quenching of the oxidation reaction was done by adding large cubes of ice (1000 ml) made through deionized water and 8ml of hydrogen peroxide (H_2O_2) was added to solution. At this step the solution encountered another color change to bright yellow. This solution was washed with deionized water. It was centrifuged at 4000 rate per minutes for fifteen minutes. An acidic wash was given to solution by addition of 1 Molar hydrochloric acid (HCl) and de-ionized water. The acid wash removed excess manganese salts as well as unwanted acids from the product. The acid washed solution pellet was washed and centrifuged at 4000rpm several times till it obtained the pH 7. Then the solution was dried overnight at 90°C to obtain the desired GO powder [83].

Graphite flakes ware provided by Asbury Carbon, NJ, Unites States. Sulfuric acid (H_2SO_4), phosphoric acid (H_3PO_4), potassium permanganate ($KMnO_4$), hydrogen peroxide (H_2O_2), hydrochloric acid (HCl), copper sulphate ($CuSO_4.5H_2O$) and iron (II) sulphate ($FeSO_4.7H_2O$) were provided by Sigma Aldrich. The chemicals obtained were reagent grade and were used without any processing. Washing and synthesis was done using deionized water.

2.8 Synthesis of Graphene Oxide Composite

The synthesis of copper ferrite/reduced graphene oxide composite was done through a one-step facile thermochemical route. 0.3 M of separately prepared Iron (II) Sulphate ($FeSO_4.7H_2O$) solution, and 0.15 M of Copper Sulphate ($CuSO_4.5H_2O$) solution were added together keeping the temperature mild, through continuous stirring for 30 minutes. The previously synthesized GO of 3.6 $mgml^{-1}$ was sonicated for 30 minutes at room temperature and mixed into the above concoction. This concoction was stirred for 90 minutes, and subsequently placed in oven overnight at 90°C.

The powder resulting from these steps was placed within a tube furnace in an argon environment, harboring a reaction temperature of 850°C for 120 minutes with heating and cooling rate of 3 °C/minute. The powder treated at the tube furnace was then homogenized through mechanical mixing and grinding to obtain the desired constituency.

The above process was repeated several times with varying weight percent of GO for each preparation. The different wt. % of sample (0%, 5%, 10% and 15%) was meant to investigate and analyze the imparted electrochemical and dielectric properties on copper ferrite through the loading effects of filler matrix [84].

Chapter 3
Characterization Techniques

After the synthesis of nanoparticles, it is important to analyze their properties through available characterization techniques. Some techniques provide an account of structural properties while others provide information regarding electric and magnetic functionalities. Our study of copper ferrite/rGO composites employ following characterization methods:

A) Morphological studies:

(i) X-Ray Diffraction Technique

❖ Porosity analysis

❖ Lattice parameter calculation and particle size

❖ Phase confirmation

❖ X-ray calculation and mass density determination

(ii) Scanning Electron Microscope

❖ Properties of surface morphology

❖ Elemental analysis

(iii) Fourier Transformed Infrared Spectroscopy

B) Electrical Characterization:

(i) Impedance Analyzer

❖ Dielectric properties

❖ DC resistivity measurement at room temperature

❖ AC conductivity

❖ AC impedance spectroscopy

3.1 X-Ray Diffraction Technique

X-ray diffraction method was first designed by W.C. Rontgen in 1985. The crystal structure is incompatible with wavelength of light wave, hence it cannot be analyzed in light rays. The wavelength of x-rays on the other hand, are almost equal to slit-size within crystal and hence provide remarkable details of phase identification within crystal structure. X-ray diffraction method gives an accurate account of structural features, atomic spacing and unit-cell dimensions in a crystal.

The technique utilizes the wave-particle duality of x-rays and employs this duality to analyze degree of crystallinity and morphology of crystal structure through diffraction patterns. This method gives its users a precise understanding of defects in crystal, average crystallite size, crystallographic orientation, phases, structural strains and degree of crystallinity. The sample is finely ground before use. Different target materials can be employed, like Cu of $K\alpha = 1.54$ (used in current study) and molybdenum. The preparation methods can be classified into powder diffraction method, rotating crystal method as well as Laue method. The powder diffraction method is utilized most commonly and encompasses the following steps:

1. Diffractometer method
2. Debye-Scherrer method (formula)

3.1.1 Working Principle of XRD

The sample is required to be finely ground into a powder form. As the X-rays interact with the finely ground sample, the plane at which x-rays are incident, act as a mirror and reflects the incident rays. The angle of this reflection is found to be equal to the angle of reflection for each set of atoms. Consequently, a constructive interference is attained in the crystal structure which can be further understood by Bragg's law equation:

$$N\lambda = 2d Sin\theta$$

Where, n is the interference order, λ denotes wavelength of incoming x-rays, d specifies interlayer distance, θ represents the angle of incoming x-rays.
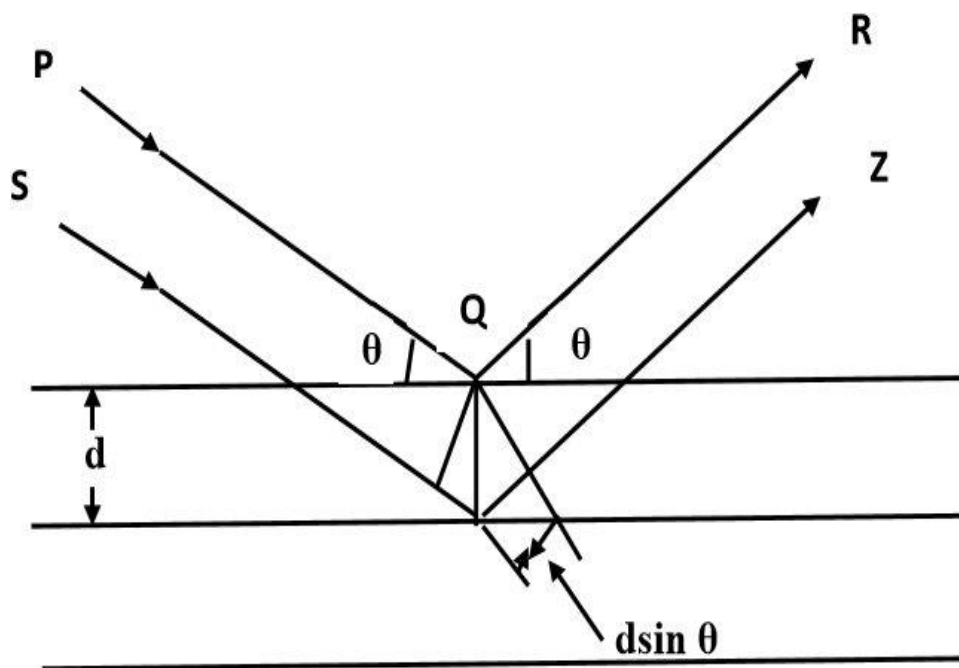
Figure 3.1: Scattering of Incident Beams of X-rays in Crystal [87]

The equation specifies that, when incident rays are incumbent on the equally spaced/distanced crystal planes and are reflected, the difference between these planes have path difference equal to $2d\sin\theta$. The value of θ is measured from the plane. Utilizing Bragg's law equation $2d\sin\theta = n\lambda$, the diffraction is achieved only when the wavelength of incident rays is smaller than 2d. Hence $\lambda < 2d$. This explains why photons from the visible light cannot be employed for this technique. Three dimensional analysis of structures can be done by using three sub-techniques namely:

(i)   Powder diffraction method

(ii)   Laue Method

(iii)   Rotating Crystal Method

The current study only employs the powder diffraction method, as the sample is finely ground to a nanopowder and the pre-requisite single crystals of optimum size are unavailable. The grounded sample is placed in a circular or rectangular shaped glass plate

or aluminum plate. As the x-rays are incident on the sample, the nanosized particles act as randomly oriented crystal. Observing a singular reflection plane, it can be observed that the nanoparticle alignment in hkl plane completely fulfils the Bragg's angle. The diffraction cone of radiation formed when θ is kept constant. Knowing the exact values of θ and λ allows for accurate calculation of interplaner spacing d.

3.1.2 Lattice Constant

Lattice parameter, also known as lattice constant is denoted as a physical dimension of unit cell residing within crystal lattice. Within the 3d (three dimensional) lattices, three lattice constants are known to exist, denoted as a, b and c. The angle between the edges or length of a single edge within the crystal is given by the value of lattice constant. It is represented by the formula:

$$a= \lambda\ (h^2+k^2+l^2)^{1/2} / 2Sin\theta$$

Where a= lattice constant, λ = wavelength of X-ray radiation (1.54 for Cu kα), H, k, l = miller indices and θ = diffraction angle.

3.1.3 Crystallite Size:

The crystallite size is parameter that receives great focus as it determines and predicts other parameters through its magnitude. The phase confirmation and phase identification is done by comparing the obtained diffractograms with JCPDS or pdf cards. Presence of broad peaks in a diffractogram pertains to the small crystallite size and vice versa. The Debye Sherrer equation proves the peak width and crystallite to be in an inverse relation to each other, as is depicted by the following relation:

$$t = \frac{0.9\lambda}{\beta\ cos\theta}$$

Here, t= crystallite size, λ =wavelength of the used X-rays, θ= diffraction angle, β= FWHM value of respective peaks.

3.1.4 X-Ray Density:

The values of x-ray density are dependent on lattice characteristics. When the value of lattice constant is known, the x-ray density can be calculated by the following formula:

$$\rho_x = ZM / N_A \, a^3$$

Here ρ_x = X-Ray density, M = molecular weight of sample, N_A = Avogadro's number (6.022×10^{-23}), a = lattice constant, Z = formula unit of cell.

X ray density studies depict that each unit cell in a spinel ferrite lattice is further divided into 8 formula units. X-ray density exists in an inverse relation with the lattice constant and a direct relationship with the molecular weight.

3.1.5 Bulk Density:

The measured density of the material is denoted by bulk density which relies on internal structure of the sample material. The sample is modified into circular pellets through a hydraulic press, in order to calculate bulk density. The value of bulk density is calculated by traditional formula for density given as:

$$\rho_m = m/\pi r^2 h$$

Here, Where ρ_m = bulk density, m = mass, r = denotes radius, h = thickness of the pressed pellet sample.

3.1.6 Porosity Fraction:

The parameter of fraction of porosity is determined through the known values of bulk density and x-ray density. It is given by the formula stated below.

$$\rho_m / \rho_x$$

Here, ρ_m = bulk density, ρ_x = X-Ray density of the sample

3.2 Fourier Transformed Infrared Spectroscopy:

The Fourier transform infrared spectroscopy allows for calculation of the absorption spectrum and emission spectrum of a liquid, solid or gas sample. The FTIR technique and the derived spectrum aids in material identification through presence of functional groups and chemical bonds.

Figure 3.2 FTIR Spectrophotometer

3.2.1 Working Principle:

The technique employs a modified interferometer. The light source emits the photons towards the interferometer and interacts with the sample compartment placed in the path. The residual light is processed by the interferometer. The light rays are modified through their interaction with the sample, and the detector measures this signal and depicts it through an interferogram. The final signal is processed by an algorithm known as Fourier transformed spectroscopy.
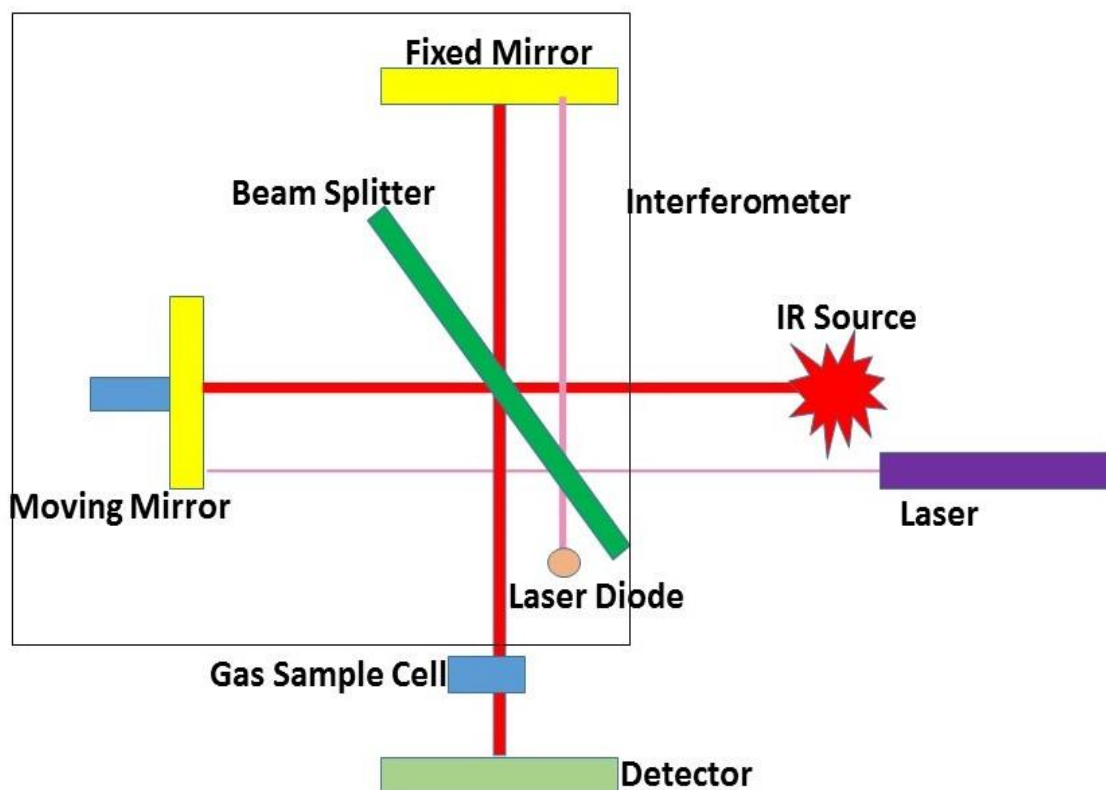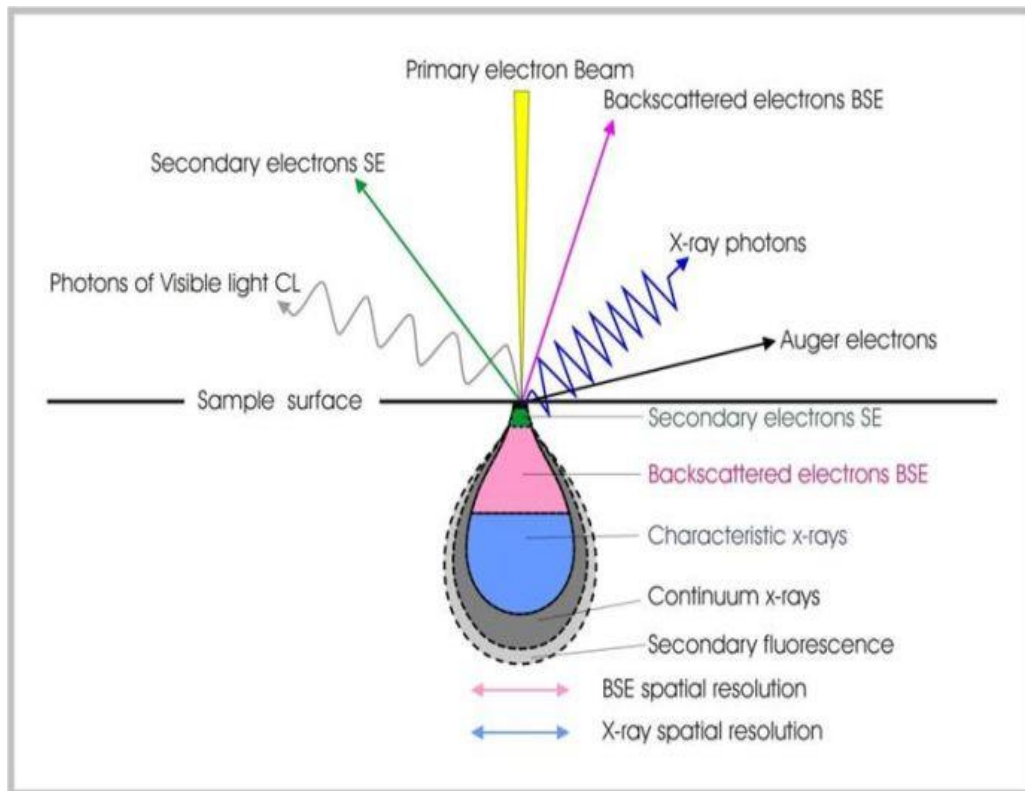
Figure 3.3 Working Principle of FTIR

3.3 Scanning Electron Microscope:

The scanning electron microscope is a device of choice that employs electron beam incident on sample to provide a scan of the morphological facets of the sample and internal details. The incident electron beam and secondary electrons produced is scanned and collected for production of an accurate sample image. SEM allows for a resolution of more than 1 nm and provides a detailed account of:

1. Sample morphology
2. Surface topography of sample
3. Phase mapping
4. Sample composition

The signal emitted from the sample are in the form of secondary electrons, transmitted and back scattered electrons, characteristic x rays as well as cathodoluminesence.

Figure 3.4 Type of Signals Produced in SEM [85]

3.3.1 SEM Working Principle:

The incident electron beam is focused on the sample through magnetic lens. The device allows for operation at high vacuum, low vacuum, a wide range of temperatures and wet or dry sample conditions. The sample area is narrow and is analyzed through a raster scan. There are two sets of lens employed in the device, the beam passage from the lens deflects them along the x axis and y axis and hence the image brightness can be tweaked through this signal. The electron amplifiers enhance the signals and present them on the screen with a differential brightness. The final image is displayed on cathode ray tube. The

incident electron beam interacts with sample and produces various signals. These signals are collected by the detectors.

The following types of images are obtained through a SEM analysis.

1. Elemental X-ray maps
2. Secondary electron images
3. Backscattered electron images
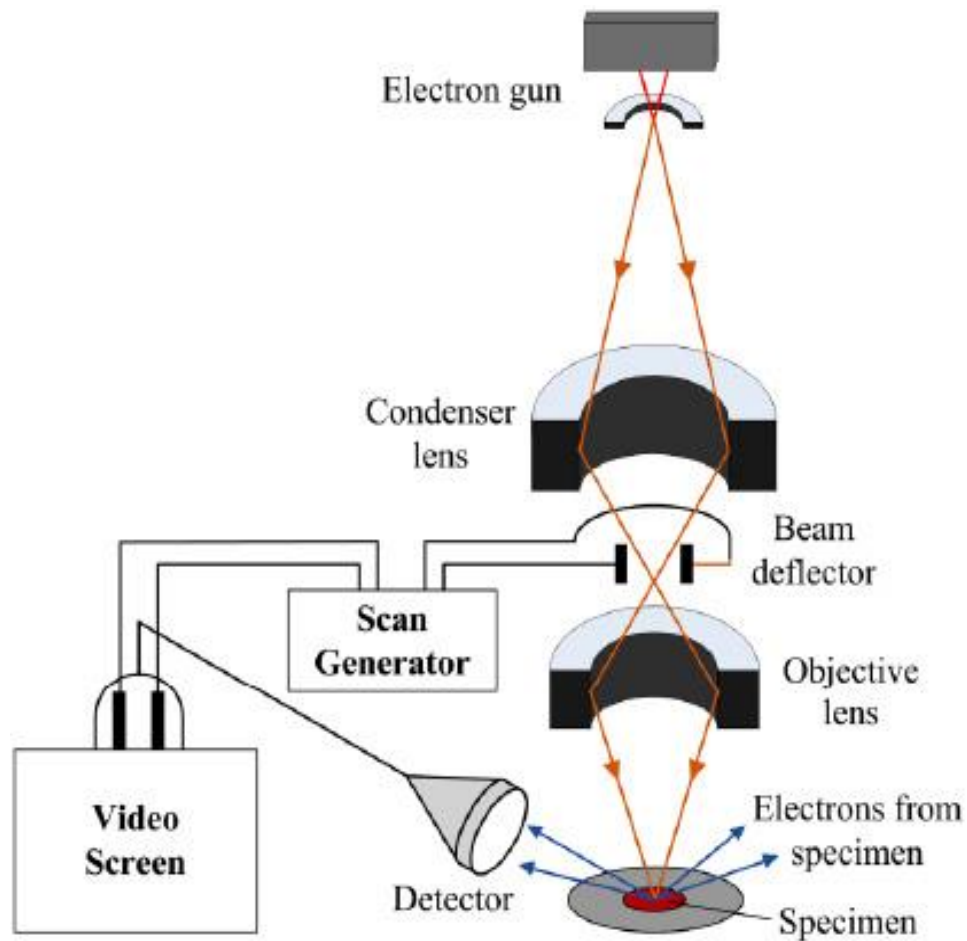
Figure 3.5: Working Schematics of SEM [86]

3.4 Dielectric Properties:

The dielectric properties of the sample was studied through the Wayne Kerr LCR 6500B device. The device meter allows for measurement of capacitance and d-factor. The dielectric characteristics of dielectric constant, dielectric loss and dielectric tangent loss. The tendency of polarization and charge storage capacity of sample is given by the dielectric constant ε' (real). The values of d factor and capacitance are utilized for the calculation of dielectric constant by the formula given as:

$$\varepsilon' = C \times t / (A \, \varepsilon \, 0)$$

Here C = capacitance of the pellet, T = thickness of the pellet, A = cross-sectional area of the flat surface of the pellet, 0 = constant of permittivity for free space. The value is given as 8.85×10^{-12} F/m.

The dielectric loss ε'' (imaginary) given an account of energy dissipation or energy loss in simpler terms. It is calculated by the formula:

$$\varepsilon'' = \varepsilon' \tan \delta$$

The dielectric parameters are best understood through Maxwell Wagner model and Koop's theory. Dielectric loss tangent factor ($\tan \delta$) is given by the ratio of dielectric loss to dielectric constant. As the field of AC is changing constantly, the dielectric material poses energy losses, which can be understood by this factor. The ratio of resistive current to charging current is another method of understanding the energy losses through dielectric loss tangent factor ($\tan \delta$). It is determined by the equation below:

$$\tan \delta = \varepsilon'' / \varepsilon'$$

3.5 AC Conductivity:

The electrical conductivity is a desirable quality in the nanomaterials, and is depicted through the physical property given by AC conductivity value. The internal process governing this phenomenon is the hopping mechanism. The conductivity in ferrites is carried out through this mechanism. The method of calculation measures the sample conductivity over a steady increment of frequency from 100 Hz to 5 MHz and are presented

by the unit S/m. Temperature is kept constant through the process. Following equation is employed to calculate the AC conductivity value:

$$\omega 0' \tan\delta$$

Here, σAC = AC conductivity, 0 = permittivity of free space, ′ = dielectric constant, tan δ = dielectric loss tangent.

3.6 AC impedance spectroscopy:

The method gives ample insight into the change within AC impedance when the frequency is shifted within the electro-ceramic composites. The real and imaginary sections of impedance are employed to make this assessment. The sample resistance and reactance are analyzed over a systematic increment of frequency from 100 Hz to 5 MHz. The temperate is kept constant. So, the resistance is the real part of calculation and the reactance is the imaginary part. Both these factors are mixed to form the actual impedance which is denoted by the SI unit Ω. The formula for calculation of impedance is given as:

$$Z = R + jX$$

Chapter 4

Results and Discussion

4.1 X-ray Diffraction (XRD) Results:

The X-ray diffraction analysis was employed to observe unit cell dimensions, crystalline structure of the synthesized $CuFe_2O_4$/rGO composite, possible presence of impurities and phase formations. This analytical method is very efficient in providing a detailed account of crystal structure, hereby acting as a confirmation step in the process of $CuFe_2O_4$/rGO nanocomposite formation. In this work, the phase formation and crystal structure were determined using X-Rays diffraction (XRD) with **θ/θ** Stoe diffractometer system at room temperature using CuKα radiation (1.5405Å).
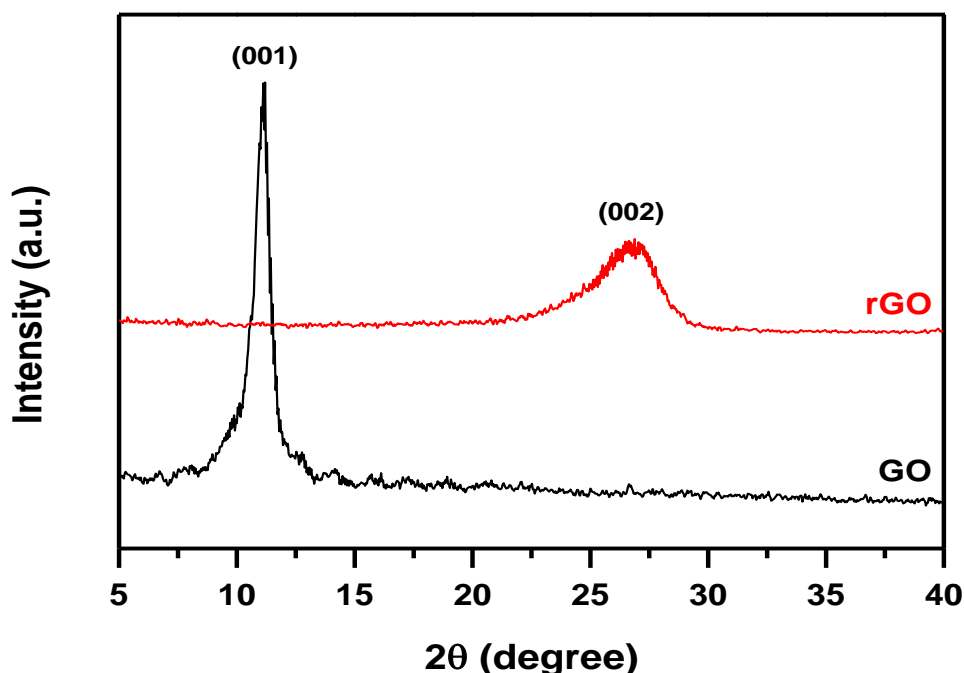

Figure 4.1: XRD of Graphene Oxide & Reduced Graphene Oxide

Figure 1 shows the XRD diffractogram of rGO & GO. The diffraction peak is observed at $2\theta=11.01^\circ$. The reflection plane (001) acted as a confirmation step for formation of graphene oxide. After the thermochemical treatment, a diffraction peak observed at $2\theta=26.8^\circ$ exhibiting reflection plane (002) acted as a confirmation step for reduction of graphene oxide and formation of rGO. This diffractogram showed a disappearance of GO peak, hereby confirming the reduction of GO into rGO. The XRD patterns of GO showed a single peak at (001) and the XRD diffractogram of rGO exhibited a single reflection peak at (002).
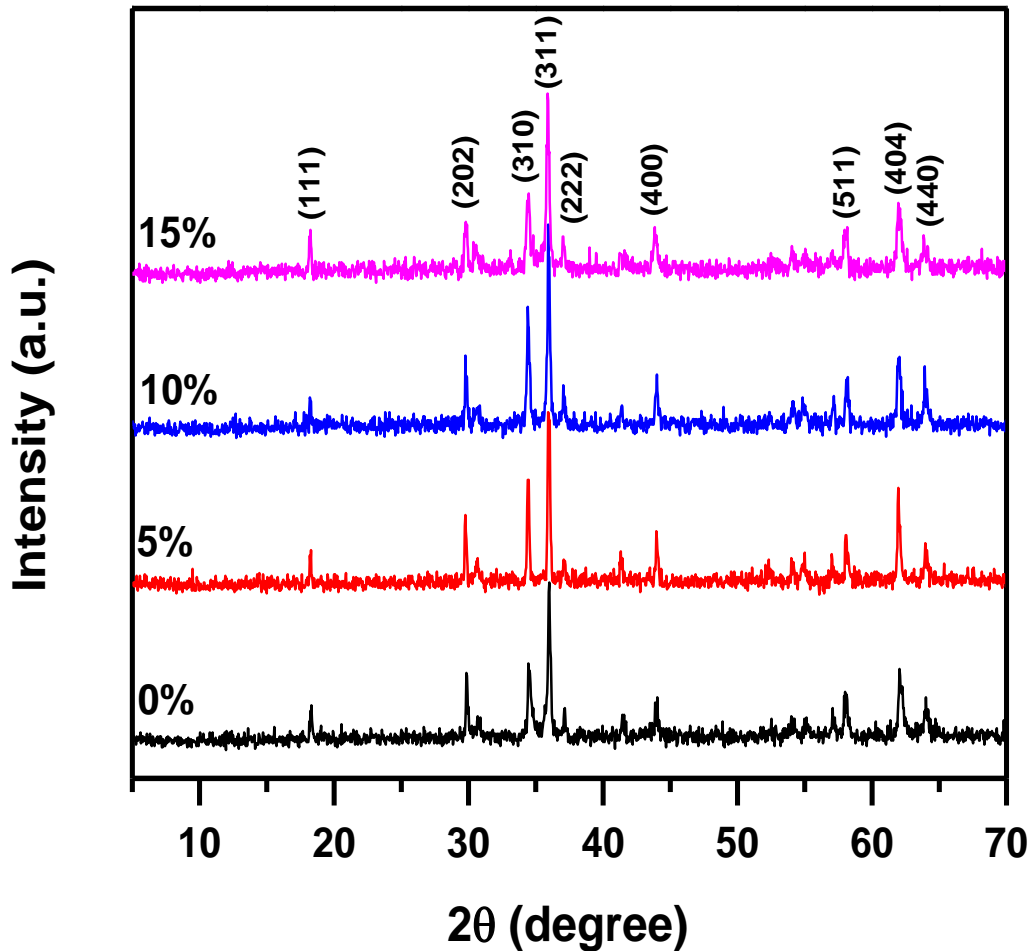

Figure 4.2: XRD of CuFe$_2$O$_4$/RGO at 0 wt. %, 5 wt. %, 10 wt. % and 15 wt. %

In figure 2, the XRD diffractogram exhibiting patterns of $CuFe_2O_4$/rGO composite as a function of GO weight percentage. The diffraction peaks were well indexed in accordance with the JCPDS card number 00-006-0545 and exhibited formation of a tetragonal structure. The diffraction peaks showed no change upon increasing the concentrations of GO from 0 wt. % to 15 wt. %. The characteristic peaks of GO and rGO were not observed within the diffractograms of the $CuFe_2O_4$/rGO composite. This confirmed the effective dispersion of graphene layers within the $CuFe_2O_4$ well up to 15 wt. % of GO. The absence of noise peaks inferred that the product had attained the desired purity, the spinel phase. This also was an indication of the suitability and efficacy of the deployed method for the synthesis of composite. The crystallite size was obtained by using Scherrer formula and was observed to be in the range of 48±6 nm.

Table 4.1: Peak Position (2θ) of the Reflection Planes of the CuFe₂O₄/rGO Composite as a Function of GO Weight Percent.

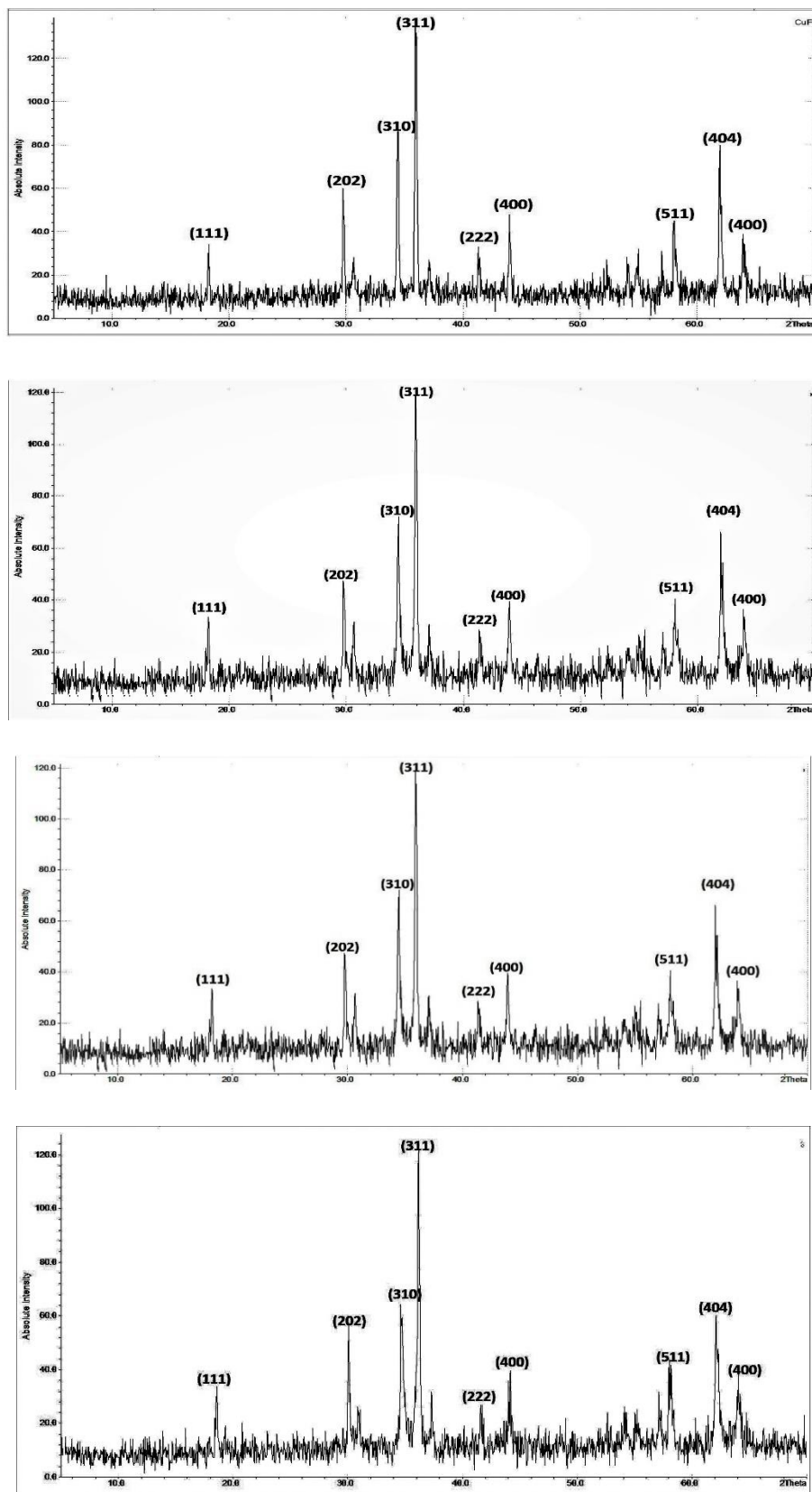| GO wt. %	2θ at (111)	2θ at (202)	2θ at (310)	2θ at (311)	2θ at (222)	2θ at (400)	2θ at (511)	2θ at (404)	2θ at (440)
0%	18.3°	29.9°	34.5°	35.9°	37.2°	44°	58°	62.1°	63.9°
5%	18.2°	29.8°	34.4°	35.9°	37.1°	43.9°	58.1°	61.9°	64.1°
10%	18.2°	29.8°	34.4°	35.9°	37.1°	43.9°	58.1°	62°	64°
15%	18.2°	29.8°	34.5°	35.8°	37.0°	43.8°	58.0°	62°	63.9°

Fig. 4.3: XRD of the CuFe₂O₄/rGO nanohybrids with increasing GO weight percent.

The XRD patterns of the $CuFe_2O_4$/rGO composite exhibit peaks at reflection planes (111), (202), (310), (311), (222), (400), (511), (404) and (440) as shown in Figure. The most intense peak was observed at reflection plane of (311) and gave a confirmation of the crystallinity of the synthesized composite. The small grain and crystallite size was confirmed by the values of the FWHM. The disappearance of GO and rGO peaks within the $CuFe_2O_4$/rGO composite exhibit the desired dispersion of graphene layers within the $CuFe_2O_4$. The characteristic peak (002) showing graphitic reflection at $2\theta = 26^o$ is not shown in any composite diffractograms indicating uniform distribution, single phase formation and complete anchorage of rGO with $CuFe_2O_4$.

Table 4.2: Variation of Average Crystallite Size (t in nm), Lattice Parameter (a in Å), Molecular Density (Dm in g/cm³), X-ray Density (Dx in g/cm³), Volume of Cell (Vcell), and Porosity (Fraction) of the CuFe₂O₄/rGO Nanocomposite as a Function of GO wt. %.

| GO wt. %	0.0%	5%	10%	15%
t (average) (nm)	42.6	49.8	51.9	53.2
a (Å)	8.3	8.2	8.2	8.2
Dm (g/cm3)	4.4	3.8	3.7	3.6
Dx (g/cm³)	5.6	5.5	5.5	5.5
Vcell (a3)	566	567	568	572
P (fraction)	0.7	0.6	0.6	0.6
P (percentage)	21.2%	30.6%	32.5%	34.1%

The conceptual introduction as provided in chapter 3 was utilized to study the unit cell of crystal. The equation of lattice constant aided in plotting a trend as a function of increasing GO concentration as shown in figure 4.4
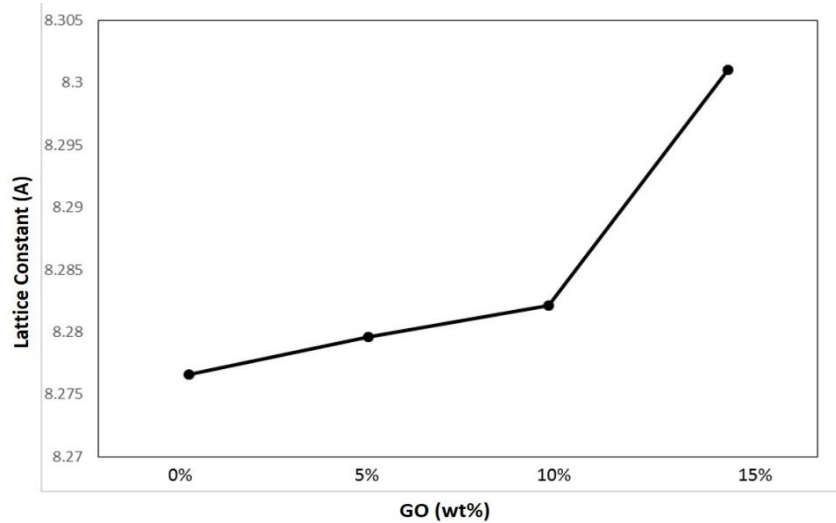
Fig. 4.4: Trend of lattice constant of CuFe$_2$O$_4$/rGO nanohybrid as a function of GOs content (weight %)

The equation for crystallite size was used and the plot of crystallite size range as a function of increase in GO weight percent was observed. The increase lies in agreement with values of FWHM. The average size was examined to be 48±6 nm. It was obtained using Debye-Scherrer's equation.
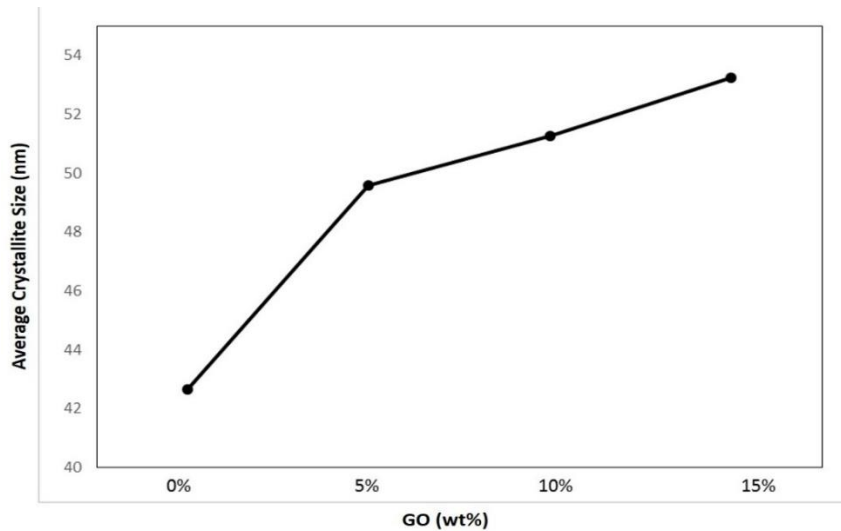
Fig. 4.5: Trend of crystallite size of CuFe$_2$O$_4$/rGO nanohybrid as a function of GO content (weight %)

The ratio of mass of unit cell to the volume of unit cell is referred as X-ray density and the ratio of mass of solid to the volume of solid is referred as mass density or bulk density.
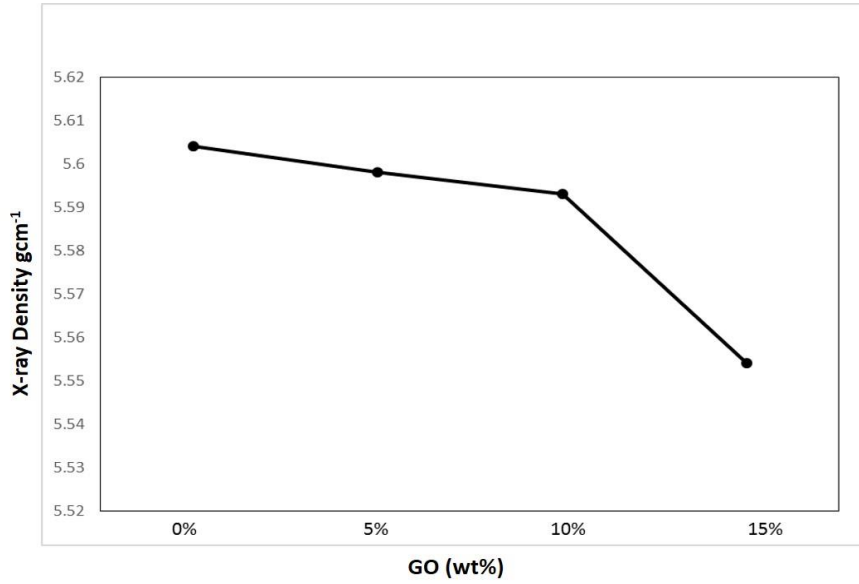
Fig. 4.6: Trend of X-ray density of CuFe$_2$O$_4$/rGO nanohybrid as a function of GO content (weight %)
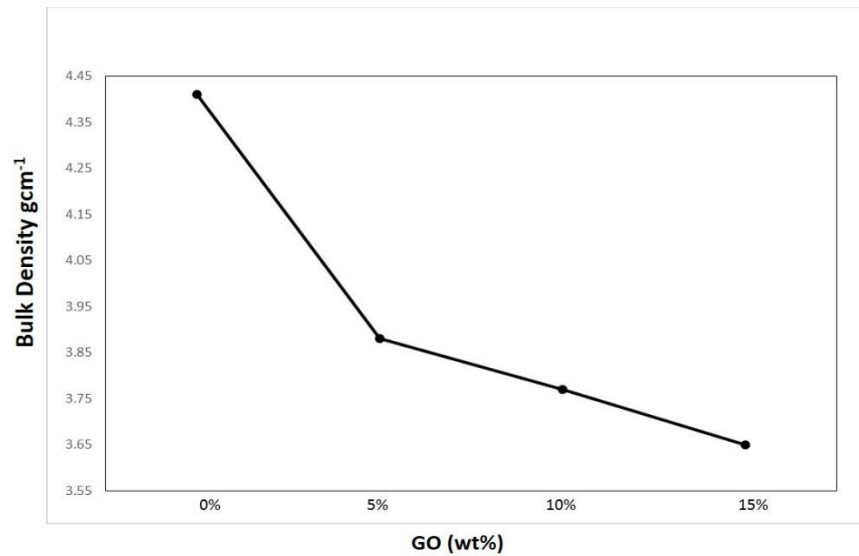
Fig. 4.7: Trend of bulk density of CuFe$_2$O$_4$/rGO nanohybrid as a function of GO content (weight %)
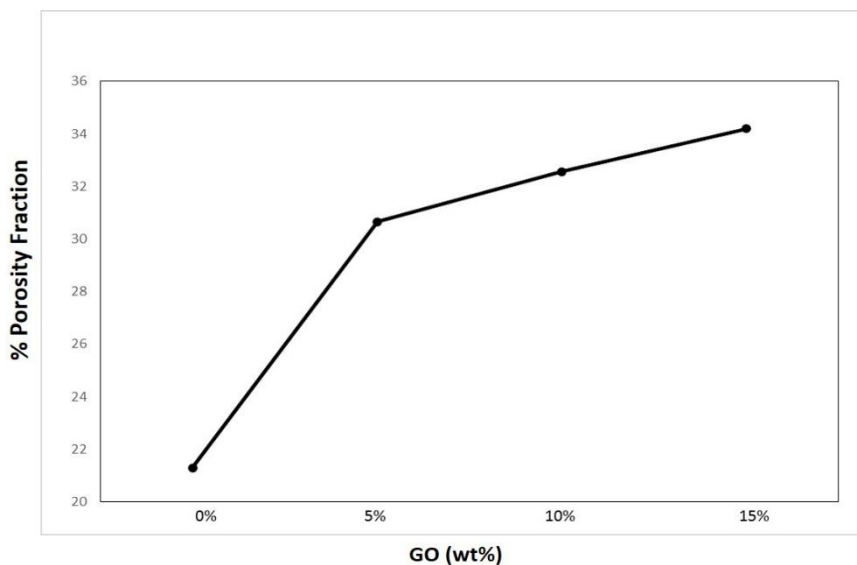
Fig. 4.8: Trend of porosity fraction of CuFe$_2$O$_4$/rGO nanohybrid as a function of GO content (weight %)

The figures 4.6 and 4.7 depict a continuous decrease in X-ray density and bulk density as a function of increasing GO weight percent. This can be attributed to the highly porous nature of graphene oxide. The GO structure is known to have an exceptional volume. Hence the decrease was expected. The increasing trend in porosity percentage is depicted in figure 4.8. This can be attributed to the increase in the interfaces of copper ferrite matrix and substantial increase in defects that renders the structure porous.

4.2 SEM Results:

The structure and surface morphology of the prepared composites and well as size distribution was determined using SEM. The sample product was prepared for the SEM analysis by sonication of the sample powder in distilled water for the period of an hour. This caused the disintegration of any clusters.

The micro structural images were taken using JEOL-JSM Scanning Electron Microscope (Model No.6390).The SEM gave the details of surface morphology of the copper ferrite nanoparticles and graphene sheets. Moreover, the nanoparticles of copper ferrite decorating the surface of rGO sheets. It can be seen that small agglomerates of nano-crystallites are anchored to rGO surface, arising as a result of inability of repulsive interaction to avoid their clustering, owing to Brownian motion and Van Der Waals attractive forces that are comparatively weak. Previously, the ferrite nanoparticles were observed to decorate the carbon nanotubes owing to the presence of driving force for reducing their surface energy. Probably, the rGO sheets act as a heterogeneous nucleating medium providing the driving force to decrease their surface energy for the nucleation of ferrite nanoparticles. The formation of agglomerates can alternatively be attributed to the dipolar nature of the copper ferrite nanoparticles.
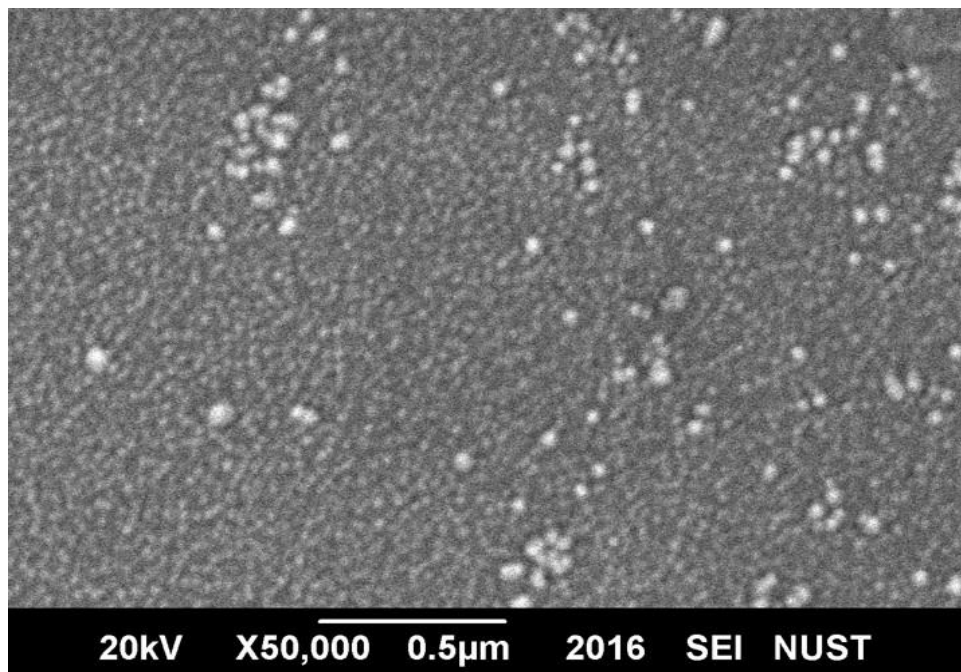
Fig. 4.9: SEM of Surface Morphology of Spherical CuFe$_2$O$_4$ Nanoparticles at X 15,000
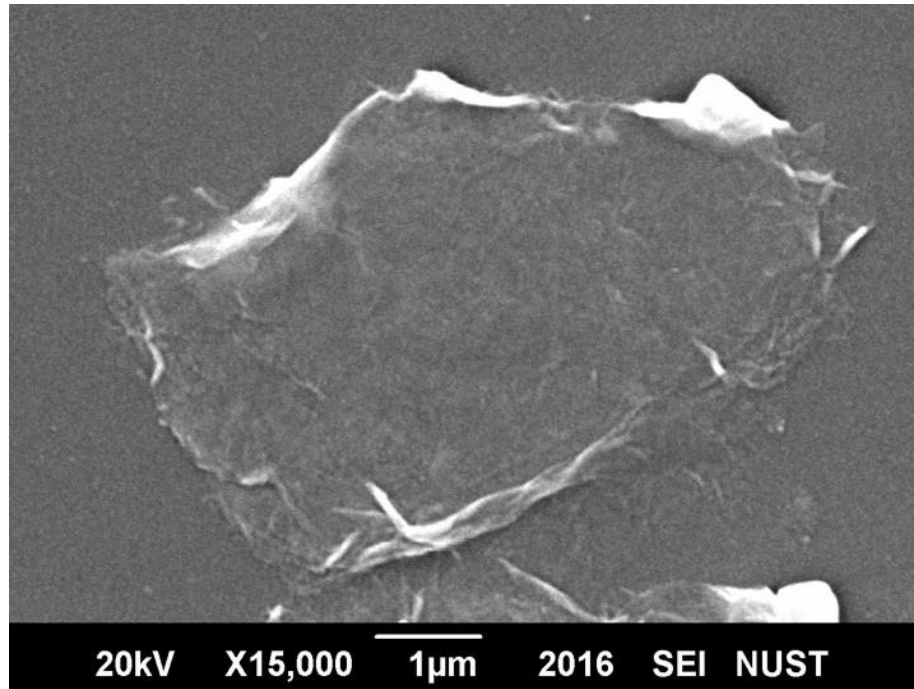
Fig. 4.10: SEM of Surface Morphology of Graphene Sheets at X 15,000
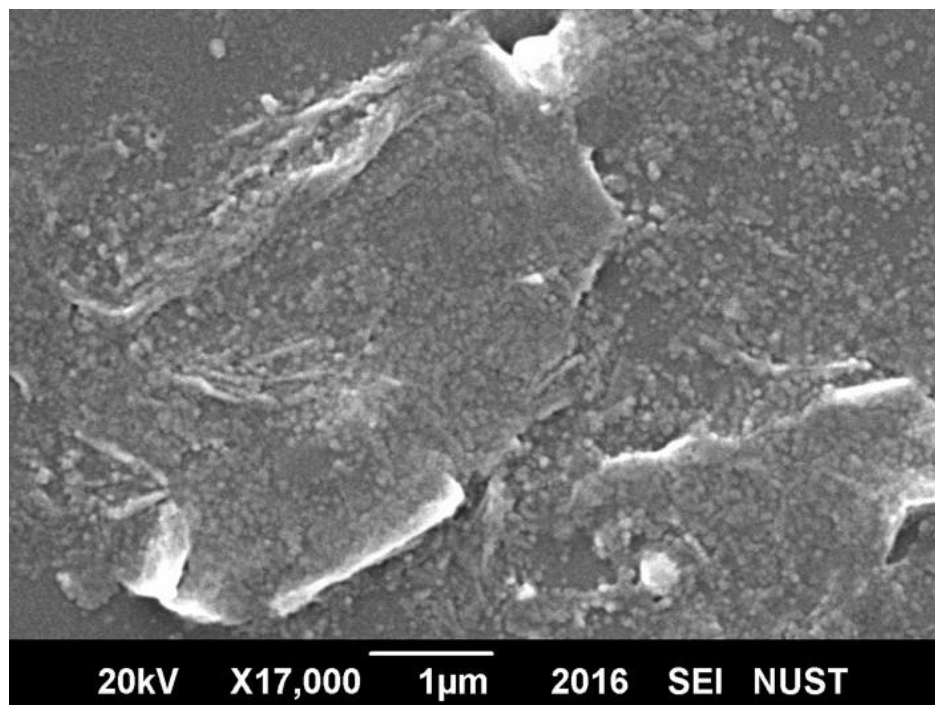
Fig. 4.11: SEM of CuFe$_2$O$_4$ Nanoparticles Coated on the Surface of RGO Sheets at X 17000

4.3 FT-IR Spectroscopy:

The sample of $CuFe_2O_4/rGO$ was prepared for FTIR analysis by subjecting them to hydraulic press pressure of four tons using kBr pellets, for a duration of three minutes. The FTIR method employs infra-red radiations. Metal-oxygen sites as well as bonding behavior were investigated by FTIR spectra (Perklin Elmer spectrum 100). The spectroscopy analysis was done at room temperature in the range of 350 cm^{-1} to 4000 cm^{-1}.The radiations correspond to the mid infrared region with range (4000~200 cm^{-1}) on the infrared spectrum, as stated below
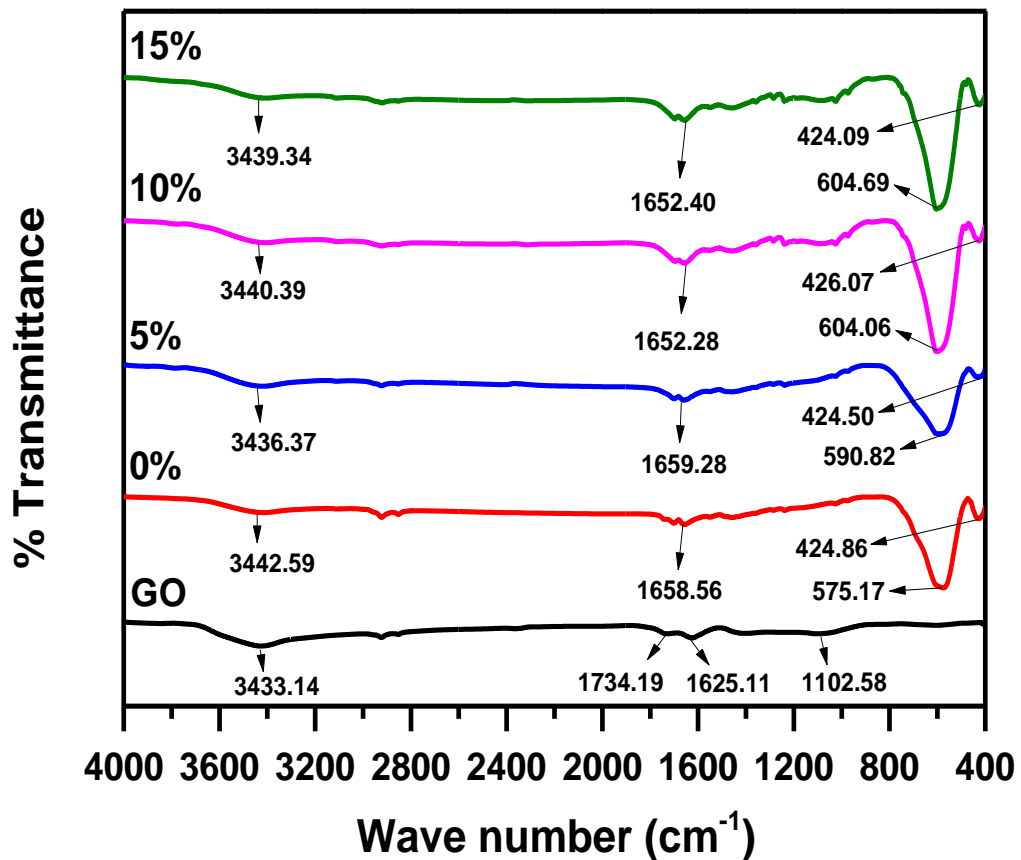

Fig. 4.12: FT-IR Spectra for GO and CuFe₂O₄/rGO Composite as a Function of GO Wt. %.

Table 4.3: Band Positions of Pristine GO and CuFe₂O₄/rGO Composite as a Function of GO Weight Percent

GO wt. %	v_1	v_2	v_3	v_4	v_5	v_6
GO	-	-	1103	1625	1734	3433
0%	425	575	-	1659	-	3443
5%	424	591	-	1659	-	3436
10%	426	604	-	1652	-	3440
15%	424	605	-	1652	-	3439

The FTIR spectra for graphene oxide GO, exhibits peaks that correspond to oxygen functionalities. This can be ascribed to, as a confirmation step for the complete oxidation of graphite. The peak at about 1730 cm^{-1} corresponds to the stretching vibration of C=O carboxyl groups. The peak at 1102 cm^{-1} corresponds to the stretching vibration of C-O. The peaks around 1625 cm^{-1} and between 2800 and 3500 cm^{-1} correspond to the functional group of O-H. 1260 cm^{-1} correspond to C- H bonds.

The lack of peaks that correspond to oxygen related functionalities within the GO spectra, confirm the reduction of GO.

The FTIR spectra of CuFe₂O₄ nanoparticles and CuFe₂O₄/rGO composites exhibited two major characteristic peaks or vibrational bands in the lattice. The bands formed around 424 cm^{-1} correspond to the vibrational mode of octahedral (B) site metal complex (bond formation between octahedral site metal ion and oxygen) while the vibrational bands around 600 cm^{-1} correspond to tetrahedral site (A) metal complex (bond formation between tetrahedral site metal ion and oxygen). The metal ion stretching, seen at higher frequency vibrational band (V1) ranges from 600-550 cm^{-1} is characteristic of a tetrahedral site-metal ion bond. The metal ion stretching at lower frequencies of absorption

band (V2) ranges at 450-385 cm^{-1} and is typical for an octahedral site-metal ion bond. Both these lattice configurations confirmed the formation of spinel structure. It is important to note that nearly similar spectra was obtained for sample preparations of different wt. % of 0%, 5%, 10% and 15%. This indicated the presence of same chemical bonds and thus confirmed the stability of the process to be utilized for the synthesis of these composites.

The results show sharp characteristic peaks/ absorption bands of spinel ferrites. All composite spectra show peaks around 424-426 cm^{-1} and 575-604 cm^{-1} and represent the octahedral and tetrahedral site respectively. The Fe-O bond length disparities at octahedral and tetrahedral sites are proposed to attribute towards the disparity in V1 and V2 absorption bands. The presence of desired product as tallied through the previously reported results is confirmed.

4.4 Dielectric behavior

4.4.1 Dielectric Constant:

The dielectric constant ε' (real part), is the measure of charge storing capacity of a material and the tendency towards polarization. Pure $CuFe_2O_4$ has dielectric constant of 3.57×10^4 at 100 Hz. A massive enhancement of dielectric constant was observed upon addition and increment of GO weight percent. The $CuFe_2O_4$/rGO composite at 5 wt. %, increased the dielectric constant to 5.42×10^4. Further increasing the GO content in $CuFe_2O_4$/rGO composite to 10 wt. %, increased the dielectric constant to 8.67×104. The $CuFe_2O_4$/rGO composite for 15 wt. % of GO showed a huge dielectric constant value of 1.27×10^5 at 100 Hz, a significant change from the initial dielectric constant. This significant enhancement of dielectric constant (at low frequency) can be attributed to the conductive nature of rGO matrix. It can be understood by Maxwell and Wagner model of space charge polarization. The model describes the ferrite solid as composed of conducting grains and resistive grain boundaries. The hopping phenomenon is utilized by electrons to reach the grain boundaries and owing to the resistive nature of these boundaries, the electrons stock or pile up here. This leads to production of polarization. The rGO exhibits a conductive nature and a large surface area, effectively acting as a parallel plate capacitor. The dipolar ferrite within the rGO matrix enhances the capacity of system to store charge through increment of stored charge contents.

The dielectric properties as a function of frequency were recorded using Wayne Kerr Precision Impedance Analyzer (Model No.6500B). The dielectric constant of the samples exhibited a decreasing trend upon increment of frequency. The larger values of dielectric constant can be observed at lower frequencies owing to the presence of all kinds of polarizations including ion, electronic and space-charge polarization. The space charge polarization is known to be higher at lower frequencies and higher temperatures. The rapid field fluctuations cause the decrease in polarizability of dipoles, causing them to lag behind in orienting themselves with the external field applied. It can understood with the help of Koop's theory which observes a dielectric material as a Maxwell-Wagner medium of two layers. The conducting grains of dielectric material in the layer are separated by insulating

grain boundary layer. The electrons perform hopping at low frequencies and agglomerate at the grain boundaries, giving rise to high permittivity. When frequency is increased, the electrons change direction and move towards opposite direction before reaching the resistive boundary, hence decreasing the dielectric constant.
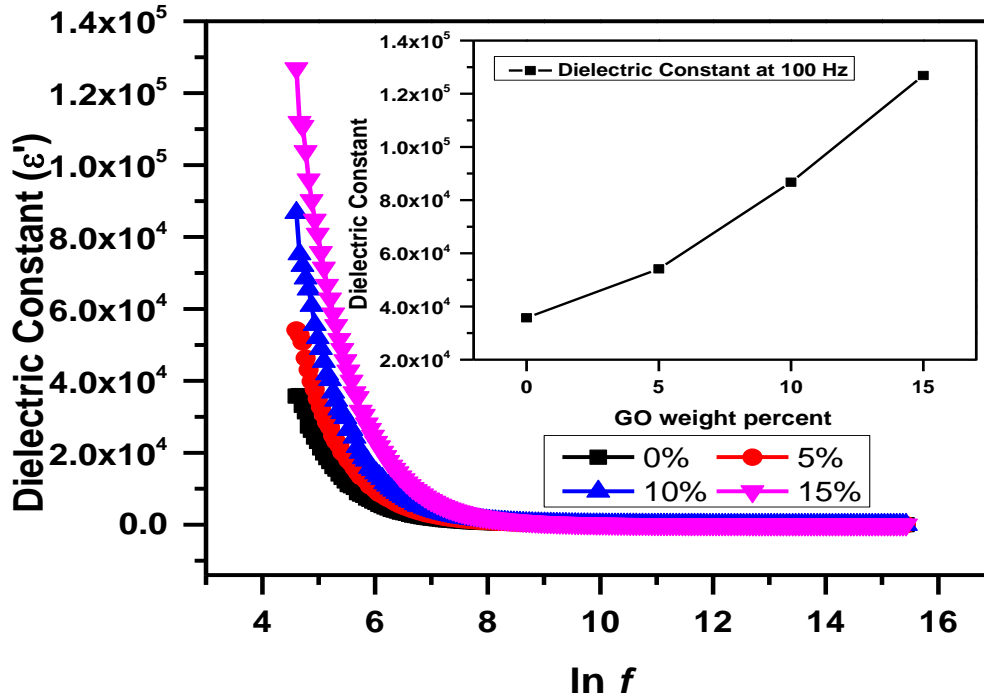

Fig. 4.13: Trend of Dielectric Constant with Frequency for CuFe$_2$O$_4$/rGO Nanocomposite as a Function of GO wt. %.

4.4.2 The Dielectric Loss:

The energy loss or energy dissipation is denoted by the dielectric loss ε'' (imaginary part). The variation of dielectric loss as a function of applied AC field is observed. This parameter follows the same trend as of dielectric constant.
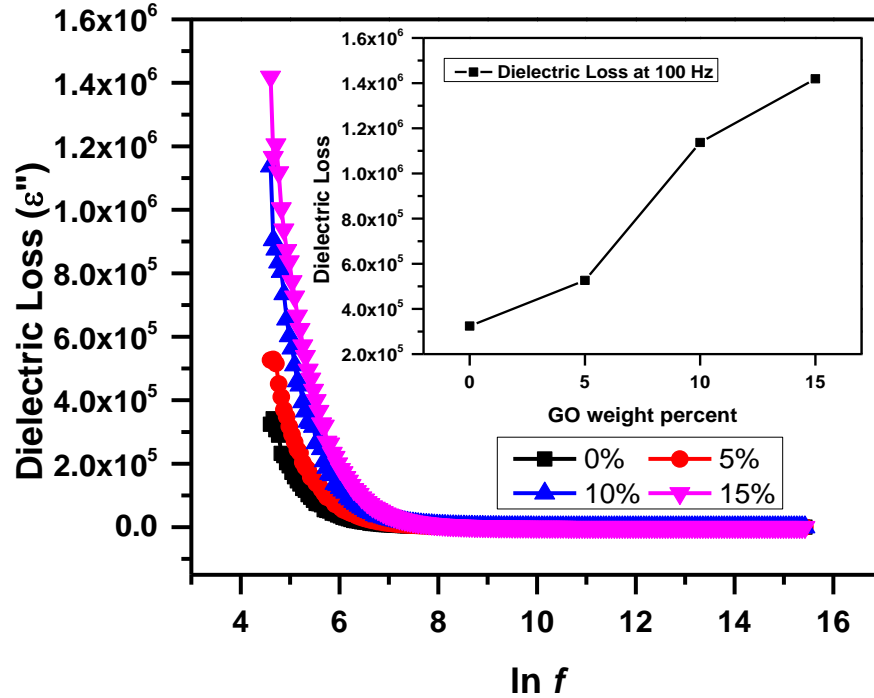
Fig. 4.14: Trend of Dielectric Loss with Frequency for CuFe$_2$O$_4$/rGO Nanocomposite as a Function of GO wt. %.

With the increase in loading of GO wt. % in the sample, the value of dielectric loss is augmented. This increase in dielectric loss with increase in concentration of GO is attributed to the emergence of defects and voids at the interface between rGO and CuFe$_2$O$_4$ matrix. For 0% GO concentration the dielectric loss was observed to be **3.24×10^5** at 100 Hz. Keeping the frequency constant, 5% GO concentration gave the dielectric loss value of **5.27×10^5.** For 10% GO concentration the dielectric loss was observed to be of **1.14×10^6.** For 15% GO concentration the dielectric loss was observed to be of **1.42×10^6** at 100 Hz. Even with the high initial values of dielectric loss at high wt. % of GO, the decreasing trend remains in line with previous observation

High ε'' values are observed at low frequency region and low ε'' values at high frequency region. This trend can be explained through Koop's theory. This space-charge polarization theory says that, well conducting grains are present within dielectric structures, flanked and separated by very thin, poorly conducting and highly resistive boundaries. The theory states that high resistivity exists, imparted by grain boundaries at low frequency. Hence, more energy is required for electrons to carry out their hopping phenomenon between Fe^{+3} and Fe^{+2} ions. Consequently, a high energy loss is observed and a voltage drop is seen.

When the frequency is increased, the resistivity of grains is reduced, and small energy is required for electrons to carry out the hopping mechanism. And energy loss is small. At higher frequency, hopping electrons cease to follow the changes in applied field after a certain limit, and hence the dielectric constant and dielectric loss values become constant.

4.4.3 Dielectric Loss Tangent:

The dielectric loss tangent factor (tan δ) is the ratio of resistive current to charging current, or more easily understood as the ratio of dielectric loss to dielectric constant. It is a measure of the relative energy loss with the alternation in the field of AC. The dielectric loss tangent shows the similar behavior of decreasing with increasing frequency, as observed with previous parameters.
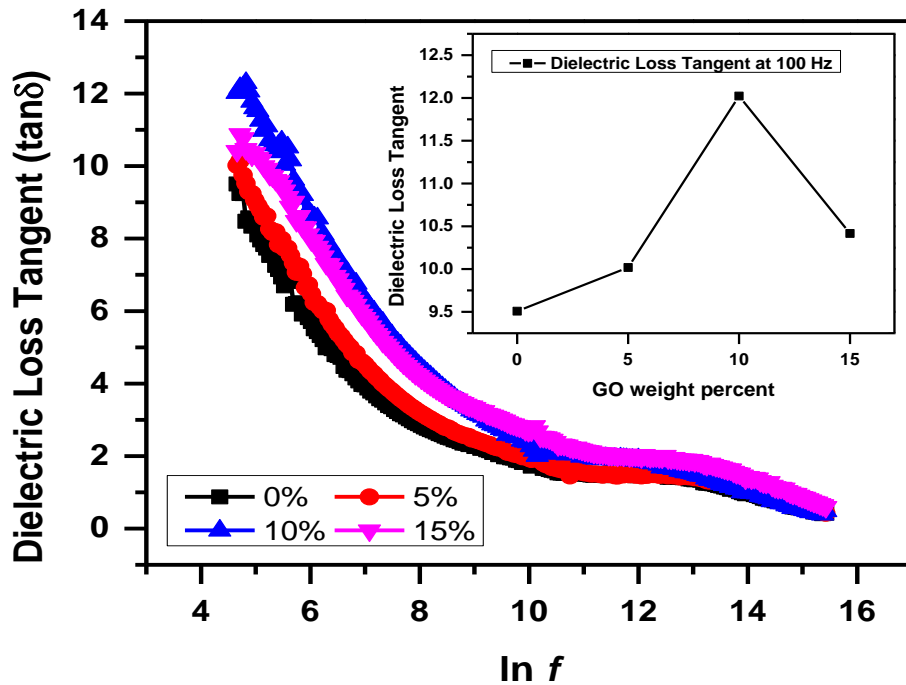
Fig. 4.15: Trend of Dielectric Loss Tangent with Frequency for CuFe₂O₄/rGO Nanocomposite as a Function of GO wt. %.

It can be observed that relative energy loss is considerably high at low frequency region. It is because of the high interruption to the passage of electric field, posed by interaction of field with majority charge carriers of dipoles. Keeping in mind the Koop's theory, this trend can be attributed to the interruption in the flow of electrons.

At low frequency, owing to the high resistivity regions (grain boundaries), the motion of electrons from Fe^{+2} and Fe^{+3} ions present at octahedral sites require more energy. Hence a higher dielectric loss tangent factor. At higher frequency, owing to the low resistivity regions (grains), the electron exchange between Fe^{+2} and Fe^{+3} ions require lesser energy. Hence the lower value of dielectric loss tangent factor. At higher frequency, the relative energy loss becomes independent of frequency, rendering the composite system suitable for high frequency, for instance high frequency microwave devices.

4.4.4 AC conductivity

AC conductivity refers to the physical property of material that allows an insight into the electrical conductivity. The conductivity in ferrites is mainly governed through the hopping phenomenon. This parameter exhibits increasing trend in low frequency region with increasing GO wt. % in line with the previously made observations.

This inclination can be attributed to the conductive nature of rGO and the prevalence of band conduction over hopping conduction. At 100 Hz frequency, the composite with 15 wt. % of GO has the highest AC conductivity values of 7.89×10^{-3} S/m and the pure copper ferrite has lowest AC conductivity values of 1.80×10^{-3} S/m. The increment of weight percent of conductive reduced graphene oxide explains this increase in conductivity.
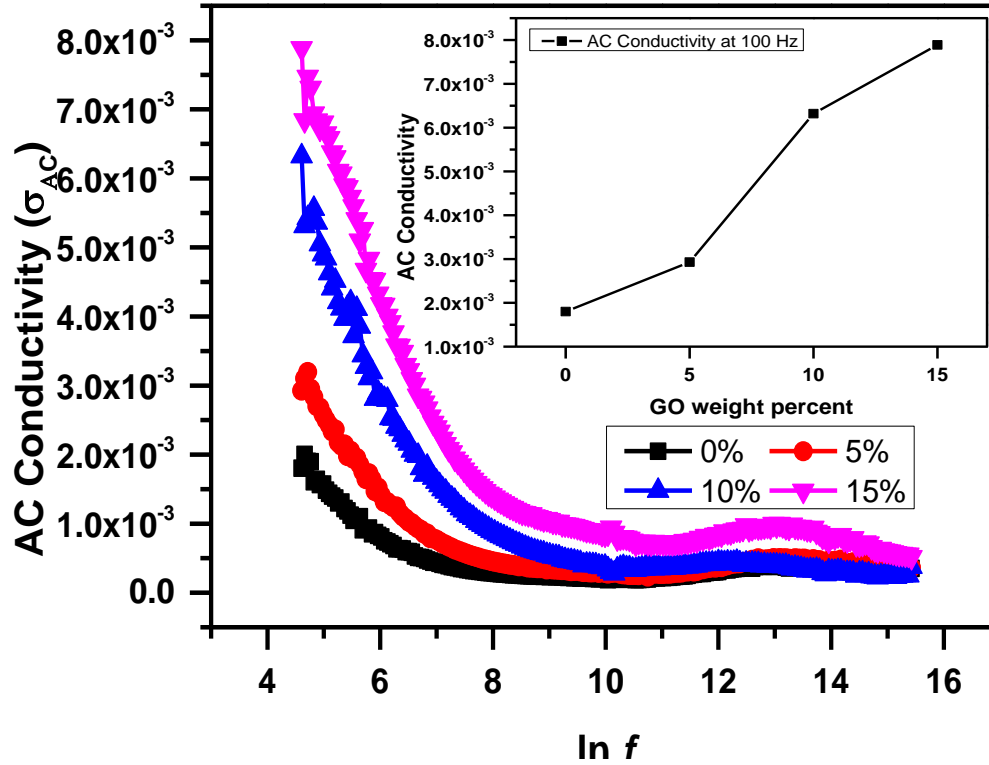
Fig. 4.16: Trend of AC Conductivity with Frequency for CuFe₂O₄/rGO Nanocomposite as a Function of GO wt. %.

Table 4.4: Variation of AC Conductivity (σAC), Dielectric Tangent Loss (Tanδ), Dielectric Constant (ε′), and Dielectric Loss (ε″) of CuFe₂O₄/rGO Nanocomposite as a Function of GO wt. %

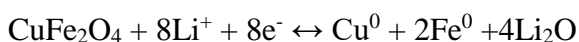| GO wt. %	0.0%	5%	10%	15%
σAC (100 Hz) s/m	1.80×10^{-3}	2.93×10^{-3}	6.32×10^{-3}	7.89×10^{-3}
Tanδ (100 Hz)	9	9.7	13.1	11.1
ε′ (100 Hz)	3.57×10^{4}	5.42×10^{4}	8.67×10^{4}	1.27×10^{5}
ε″ (100 Hz)	3.24×10^{5}	5.27×10^{5}	1.14×10^{6}	1.42×10^{6}

4.5 Electrochemical performance:

The electrochemical properties were measured by galvanostatic charge-discharge testing against lithium as the counter electrode. The working electrodes were made by a slurry coating procedure in which slurry was prepared by sonicating 80 wt. % of sample material, 10 wt. % of acetylene black and 10 wt. % of poly (vinylidenefluoride) PVDF binder in N-methyl pyrrolidinone solvent. Slurry was then uniformly coated on the copper foil current collector. The electrodes were dried in a vacuum oven at 100 °C for 12 h. A CR-2032 type coin cell was fabricated in an argon filled glove box using polyethylene as a separator and 1 mol/L LiPF6 in ethylene carbonate/dimethyl carbonate (1:1) as the electrolyte. The electrochemical charge-discharge tests of the sample were performed at voltage limits of 3.0-0.01 V versus Li/Li$^+$.
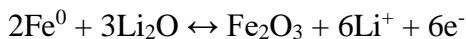
The electrochemical performance was assessed to analyze the influence of graphene matrix on CuFe$_2$O$_4$/rGO composite. The charge discharge curves of pure CuFe$_2$O$_4$ and CuFe$_2$O$_4$/rGO composite for 15 wt. % of GO at current density of 100 mA g^{-1} were measured. The curves demonstrate the oxidation and reduction reactions during the steps of lithium insertion and extraction. The charging curves lay testimony to the linear increase of charging capacity with increasing voltage. It is attributed to the insertion of Li$^+$ ions into CuFe$_2$O$_4$. The voltage plateau occurs at 1.3 V. This shows the presence of copper ferrite.

As the voltage drops, the discharge curves exhibit the first voltage plateau at around 3 and 1.3 V, due to the ohmic polarization and formation of solid electrolyte interface. The second plateau was observed at around 1.3 and 0.8 V and was attributed to the reactions at electrolyte interface. The last plateau occurred at around 0.8 and 0.01 V and was allocated to the mass transport limitation which causes a deformation of the material structure and formation of Cu and Fe scattered in a matrix of Li$_2$O.

The underlying electrochemical reactions are given as:

$$CuFe_2O_4 + 8Li^+ + 8e^- \leftrightarrow Cu^0 + 2Fe^0 + 4Li_2O$$

$$Cu^0 + Li_2O \leftrightarrow CuO + 2Li^+ + 2e^-$$

$$2Fe^0 + 3Li_2O \leftrightarrow Fe_2O_3 + 6Li^+ + 6e^-$$

Specific Capacity of Pure CuFe$_2$O$_4$

The first charge and discharge cycles of pure CuFe$_2$O$_4$ gave the specific capacity of 660 mAh g^{-1} for charge cycle and the specific capacity of 900 mAh g^{-1} for discharge cycle. The columbic efficiency for pure CuFe$_2$O$_4$ was 73.3%. In the preceding second cycle the specific capacity was calculated as 670 mAh g^{-1} and for the fifth cycles, the value was 640 mAh g^{-1}.

Specific capacity of CuFe$_2$O$_4$/rGO Composite

The first charge and discharge cycles of CuFe$_2$O$_4$/rGO composite gave the specific capacity for charge cycle as 895 mAh g^{-1} and the specific capacity for discharge cycle as 1190 mAh g^{-1}. The columbic efficiency for CuFe$_2$O$_4$/rGO composite was 75.2%. %. In the preceding second cycle the specific capacity was calculated as 910 mAh g^{-1} and for the fifth cycles, the value was 865 mAh g^{-1}. Factors like, structural defects in the composite, existence of oxygen functionalities and large surface area facilitate the insertion and de-insertion of Li$^+$ ions into voids free spaces. This is the rationale behind the increase in the specific capacity.

Cyclic Stability of Pure CuFe$_2$O$_4$:

The cyclic stability of pure CuFe$_2$O$_4$ at current density of 100mAh g^{-1} was examined. The electrode delivered a capacity of 900 mAh g^{-1} at the first cycle and 625 mAh g^{-1} 25th cycle.

Cyclic Stability of CuFe$_2$O$_4$/rGO Composite

The cyclic stability of CuFe$_2$O$_4$/rGO composite for 15 wt. % of GO at current density of 100mAh g^{-1} was examined. The electrode delivered a capacity of 1200 mAh g^{-1} at the first cycle and 845 mAh g^{-1} 25th cycle.

The increase in cyclic stability is proposed to be attributed by rGO. RGO provides good electronic conductivity, large surface area, porosity and excellent adhesive properties in the sample. These factors provide enough space to buffer the volume change during the Li$^+$ ion insertion and extraction reactions in CuFe$_2$O$_4$ nanoparticles.

Rate Capacity of Pure CuFe₂O₄

The rate capability of pure $CuFe_2O_4$ at different current densities was examined. The calculated value of reversible capacity at each current rate remains constant and stable.

- ❖ 670 mAh g^{-1} was delivered at 100 mA g^{-1} current density
- ❖ 655 mAh g^{-1} was delivered at 200 mA g^{-1} current density
- ❖ 630 mAh g^{-1} was delivered at 500 mA g^{-1} current density
- ❖ 540 mAh g^{-1} was delivered at 1000 mA g^{-1} current density
- ❖ 425 mAh g^{-1} was delivered at 2000 mA g^{-1} current density

These results were obtained for 30 cycles.

Rate Capacity of CuFe₂O₄/rGO Composite:

The rate capability of $CuFe_2O_4$/rGO composite for 15 wt. % of GO at different current densities was examined. The calculated value of reversible capacity at each current rate remains constant and stable.

- ❖ 870 mAh g^{-1} was delivered at 100 mA g^{-1} current density
- ❖ 850 mAh g^{-1} was delivered at 200 mA g^{-1} current density
- ❖ 840 mAh g^{-1} was delivered at 500 mA g^{-1} current density
- ❖ 730 mAh g^{-1} was delivered at 1000 mA g^{-1} current density
- ❖ 510 mAh g^{-1} was delivered at 2000 mA g^{-1} current density

At the current density of 100 mA g^{-1}, specific capacity returned back to 650 for pure $CuFe_2O_4$ and 860 mAh g^{-1} for $CuFe_2O_4$/rGO composite, indicating the 100% capacity retention. The increase in rate capability can be attributed by the short diffusion path for Li^+ ions in electrolyte. As $CuFe_2O_4$ nanoparticles are embedded into rGO sheets which prevent $CuFe_2O_4$ from aggregating and providing good electronic conductivity. The enhanced conductivity and surface area provide fast transfer of electrons through rGO matrix which results in shorter pathway for Li^+ ion diffusion during the Li^+ ion insertion and extraction reaction.
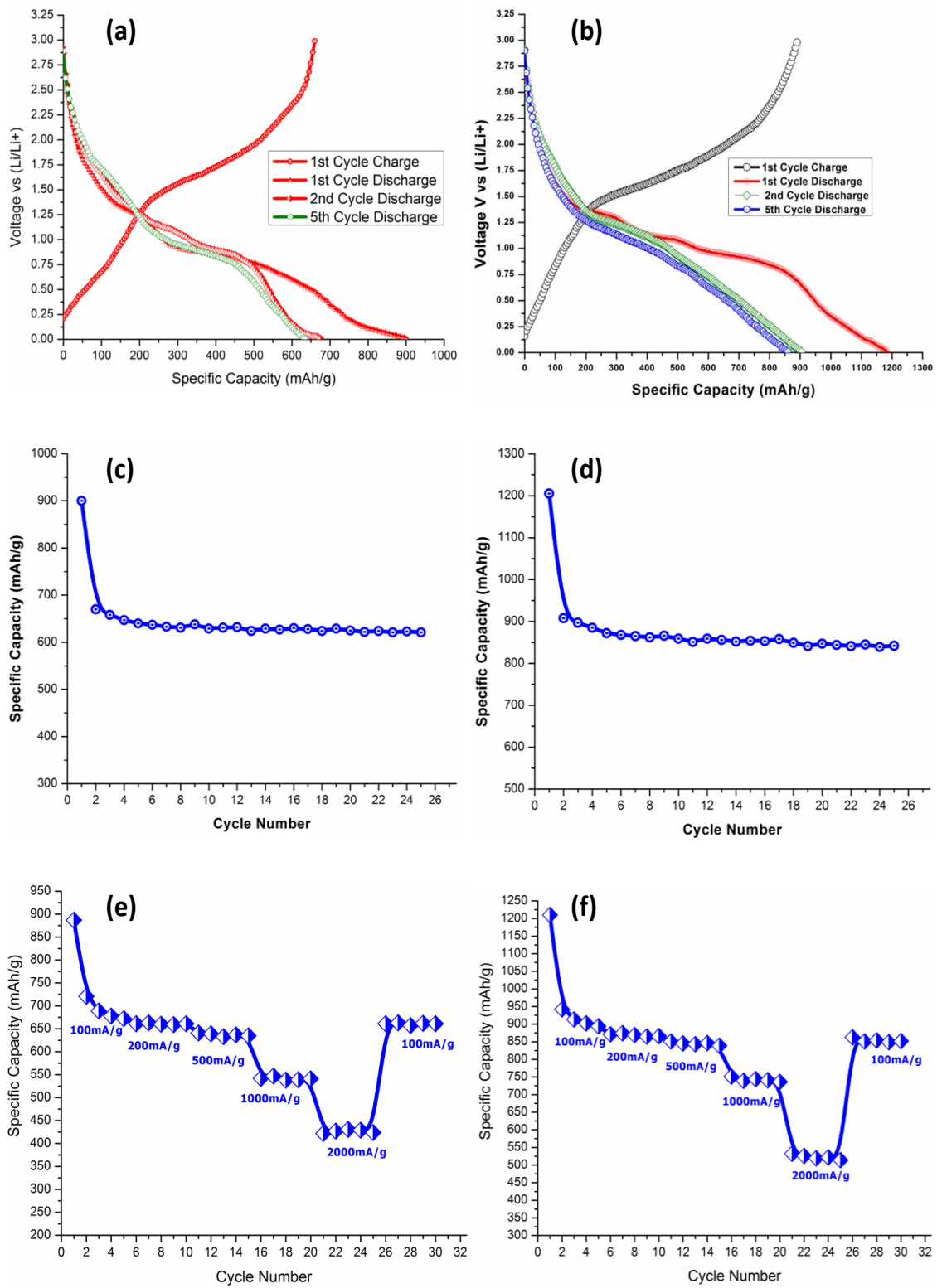
Figure 4.17: Variation in Specific Capacity, Cyclic Stability and Rate Stability of CuFe₂O₄/rGO Compared with CuFe₂O₄

4.6 Conclusion

The research study employed a novel, facile one step thermochemical reaction for the synthesis of $CuFe_2O_4$/rGO composite system. The techniques utilized for the characterization for these hybrid systems (XRD & SEM) confirm the efficiency of this novel one step method. They demonstrated a flawless, rough tethering of $CuFe_2O_4$ on rGO sheets. The absence of extra peak has been observed in XRD and FTIR measurements proved the absence of impurities and retention of affecting the spinel structure of $CuFe_2O_4$. The structural formation of ferrite was also confirmed by FTIR Spectra, showing band ranges of 575 cm^{-1} to 605 cm^{-1} for tetrahedral and 424 cm^{-1} to 427 cm^{-1} for octahedral lattice sites. The SEM images clearly show successfully decoration of copper ferrite nanoparticles on rGO sheets. The dielectric properties were massively enhanced through addition of rGO in copper ferrite. All the parameters of dielectric properties encompassing dielectric constant, dielectric loss, tangent loss and AC conductivity showed enhancement with increment of weight percentage of GO. For 15 wt. % of GO, the dielectric constant increased from 3.57×10^4—1.27×10^6. Similarly dielectric loss and tangent factor increased from 3.24×10^5—1.42×10^6 and 9.0737—11.1848, respectively at 100 Hz. This observation indicated the potential of the $CuFe_2O_4$/rGO composites for applicability in supercapacitors. The AC conductivity increases from 1.80×10^{-3} to 7.89×10^{-3} S/m at 100 Hz. The Specific capacity increased from 900—1190 mAh g^{-1} while cyclic stability increased from 625—845 mAh g^{-1} after 25 cycles at current density of 100 mA g^{-1}, respectively. This unique approach of embedding $CuFe_2O_4$ on rGO sheet yields high performance electrode material for lithium-ion batteries.

4.7 Future Prospects:

The future prospects of any novel composite system relies on the applicability it provided, and the demand of that application in view of the current global scenario. The most pressing energy challenges of today include fast depletion of fossil reserves, as well as dependence of energy systems on the renewable reserves. The developing countries, like Pakistan, are also significantly affected by the cost-effectivity offered by novel methods as well as the efficiency of the system. Thus, the current scenario of energy crises needs to be met with a system that caters to a plethora of parameters that inspire a wide scale commercialization. The currently developed composite can be further exploited with increasing weight percent of GO. Also, other characterization methods available can be utilized for in depth structural analysis. The potential applications in the field of these systems can be looked into. The synthesis protocols can be further optimized for cost reduction and simplicity. Moreover, the properties and parameters of these systems can optimized for better and newer results.

References:

1. Snelling E C, Soft ferrites and Applications, Butterworths Publishing, London, UK, 2 nd Edition, (1989).
2. Kools F, Hard magnetic ferrites-In concise Encyclopedia of Advanced Ceramic materials, Pergamon Press, Oxford (1991).
3. Groenou V, et al, Materials Sci. and Engg., 3 (1968/69) 317-342
4. Adams D M, Inorganic Solids, John Wiley: London, 1 st Edition (1974).
5. Sickafus K E and Wills J, J. Am. Ceram. Soc., 82 (1999) 3279-3292
6. Brag W H, The structure of the spinel group of crystals, Philosophical Magazine, 30 (1915) 305-315.
7. Smit, J. Wijn, H. P. J. Ferrites-Physical Properties of Ferrimagnetic Oxides in Relation to their Technical Applications, John Wiley and Sons, Netherlands, (1959).
8. Guinier A, X-Ray Diffraction: In Crystals, Imperfect Crystals and Amorphous Bodies, Unabridged Dover publications, Freeman & company Ltd., San Fransisco, (1994)
9. Li F.S., Wang L., Wang J.B., Zhou Q.G., Kunkel H.P., Williams G., Magn J., Magnmater.268 (2004)
10. Neel L., magnetic properties of ferrites, Ferrimagnetism and antiferromagnetism, Ann.phys.paris, 3(1948)
11. Livingston J. D., "A review of coercivity mechanism", Appl.phys (1981), 522-541.
12. Lal R., Suman, Sharma N.D.,Taneja S.P. , and Reddy V. R., Ind. J. Pure and Appl. Phys. 45 (2007).
13. Singhal S., Barthwal S.K., and Chandra K., J. Magn. Magn. Mater. 296, (2006).
14. Pandit A.A., Shitre A. R.,Shengule D.R., and Jadhav K.M., J. Mater. Sci. 40 (2005).
15. Singhal S, Singh J.,Barthwal S.K., and Chandra K., J. Solid State Chem. 178 (2005).
16. Joseyphus R. J.,Narayanasamy A., Shinoda K., Jeyadevan B., and Tohji K., J. Phys. Chem. Sol. 67 (2006).
17. Hastings J. M. and Corliss L.M., Phys. Rev. 104 (1956) 328.
18. Dhiman R.L., Taneja S.P., and Reddy V. R. , Adv. Cond. Matter Phys. 2008 (2008).
19. Shrotri J.J., Kulkarni S.D.,Deshpande C.E, Mitra A., Sainkar S.R., Anil P.S., Kumar, Date S.K, Mater. Chem. Phys. 59 (1999).
20. Spaldin N., magnetic materials, fundamental and device applications, Cambridge: Cambridge university press, 2003.
21. Standely K.J., "Oxide magnetic materials" 2nd edi., Oxford university press, (1972)
22. Sinha A.P.B and Menon P.G., "Oxide Magn. Mater." National Chemical Laboratory Poona, India.

23. Rafferty A., Prescott T.,Brabazon D., "Sintering behaviour of cobalt ferrite ceramic",Ceramics International 34 (2008).
24. Kato V.,Takei T., J.Inst.Elect.Engrs.53 (1933).
25. Kawai M., J, Soc.Che.Ind.Jpn.37, (1934).
26. Snock J.L., physics 3, (1936).
27. Neal L. Ann.phys 3, (1948).
28. Snock J.L. Non-metalic magnetic materials for high frequency, Philips.Tech.Rev. 8(1946).
29. Polder D. On the Theory of Ferromagnetic Resonance. phil.mag. 40(1949).
30. Hogan C.L.The microwave gyrator. J.Bell system tech., 31(1952).
31. Gopalakrishnan G., Wilcke W., McCloskey B., Luntz A., and Swanson S., J. Phys. Chem. Lett., 1, 2193 (2010).
32. Abouimrane A., Compton O.C., Amine K., and Nguyen S.T., J. Phys. Chem. C, 114, 12800 (2010).
33. Zhu N., Liu W., Xue M. Q., Xie Z., Zhao A, D., Zhang M. N., Chen J. T., and Cao T. B., Electrochim Acta, 55, 5813 (2010).
34. Bhardwaj T., Antic A., Pavan B., Barone V., and Fahlman B. D., J. Am. Chem. Soc., 132, 12556 (2010).
35. Lian P. C., Zhu X. F., Liang S. Z., Li Z., Yang W. S., and Wang H. H., Electrochim. Acta, 55, 3909 (2010).
36. Wang G. X., Shen X. P., J. Yao, and J. Park, Carbon, 47, 2049 (2009).
37. Pan D. Y., Wang S., Zhao B.,Wu M. H, Zhang H. J., Wang Y., and Jiao Z, Chem. Mater., 21, 3136 (2009).
38. Wang C. Y., D. Li, C. O. Too, and G. G. Wallace, Chem. Mater., 21, 2604 (2009).
39. Liang M. H. and. Zhi L. J, J. Mat. Chem., 19, 5871 (2009).
40. Yoo E., Kim J., Hosono E., Zhou H,, Kudo T., and Honma I., Nano Lett., 8, 2277 (2008).
41. Uthaisar C. and Barone V., Nano Lett., 10, 2838 (2010)
42. Pollak E. , Geng B. S., Jeon K. J., Lucas I. T., Richardson T. J., Wang F., and Kostecki R., Nano Lett., 10, 3386 (2010).
43. Fu L. J, Liu H., Li C., Wu Y. P., Rahm E., Holze R., and Wu H. Q., Solid State Sci., 8, 113 (2006).
44. Lightcap I. V., Kosel T. H., and Kamat P. V., Nano Lett., 10, 577 (2010).
45. Williams G., Seger B., and Kamat P. V., ACS Nano, 2, 1487 (2008).
46. Poole. Jr. C P and Owens F J, Introduction to Nanotechnology, Wiley, John & Sons, (2003).
47. Wolf E L, Nanophysics and Nanotechnology: An Introduction to Modern, Concepts in Nanoscience, Wiley, John & Sons, 2nd Edition, (2006).
48. Ramsden, J, Nanotechnology: An Introduction, Elsevier, Amsterdam (2011).
49. Feyman R P, J. Micro-electrochemical Systems, 1(1992) 60-66.
50. Barack, O. "Remarks by the President at the National Academy of Sciences Annual Meeting", Washington, DC, April 27, (2009)
51. Collins, F. "Opportunities for research and NIH", Science 327, (2010)

52. Kuhn, T. "The structure of scientific revolutions". Third Ed. UoC Press (1996)
53. Sartale S.D., Lokhande C.D., Muller M., Electrochemical synthesis of nanocrystalline CuFe2O4 thin films from non-aqueous (ethylene glycol) medium, Mater. Chem. Phys. 80 (2003)
54. Sultan M., Singh R. Magnetization and crystal structure of RF-sputtered nanocrystalline CuFe2O4 thin films, Mater. Lett. 63 (2009)
55. Ponhan W., Maensiri S. Fabrication and magnetic properties of electrospun copper ferrite (CuFe2O4) nanofibers, Solid State Sci. 11 (2009)
56. Barreto J. A., O'Malley W., Kubeil M., Graham B., Stephan H., and Spiccia L., "Nanomaterials: applications in cancer imaging and therapy," Advanced Materials, vol. 23, (2011).
57. Chopra N., Gavalas V. G., Bachas L. G., Hinds B. J., and Bachas L. G., "Functional One-Dimensional Nanomaterials: Applications in Nanoscale Biosensors," Analytical Letters, vol. 40, pp. 2067-2096, (2007).
58. Pankhurst Q. A., Connolly J., Jones S. K., and Dobson J., "Applications of magnetic nanoparticles in biomedicine," Journal of physics D: Applied physics, vol. 36, p. R167, (2003).
59. Li Q., Mahendra S., Lyon D. Y., Brunet L., Liga M. V., Li D., et al., "Antimicrobial nanomaterials for water disinfection and microbial control: potential applications and implications," Water research, vol. 42, pp. 4591-4602, (2008).
60. Hazra S. and Ghosh N., "Preparation of nanoferrites and their applications," Journal of nanoscience and nanotechnology, vol. 14, pp. 1983-2000, (2014).
61. Mathur P., Thakur A., Lee J., and Singh M., "Sustained electromagnetic properties of Ni–Zn–Co nanoferrites for the high-frequency applications," Materials Letters, vol. 64, pp. 2738-2741, (2010).
62. Dar M. A., Verma V., Gairola S., Siddiqui W., Singh R. K., and Kotnala R., "Low dielectric loss of Mg doped Ni–Cu–Zn nano-ferrites for power applications," Applied Surface Science, vol. 258, pp. 5342-5347, (2012).
63. Herzer G., "Nanocrystalline soft magnetic materials," Physica Scripta, vol. 1993, p. 307, (1993).
64. Makino A., Hatanai T., Inoue A., and Masumoto T., "Nanocrystalline soft magnetic Fe-MB (M= Zr, Hf, Nb) alloys and their applications," Materials Science and Engineering: A, vol. 226, pp. 594-602, (1997).
65. Buschow K., "New developments in hard magnetic materials," Reports on Progress in Physics, vol. 54, p. 1123, 1991.
66. Callister W. D. and Rethwisch D. G., Materials science and engineering vol. 5: John Wiley & Sons NY, (2011).
67. Morin F., "Oxides which show a metal-to-insulator transition at the Neel temperature," Physical Review Letters, vol. 3, p. 34, (1959)
68. Bedanta S. and Kleemann W., "Supermagnetism," Journal of Physics D: Applied Physics, vol. 42, p. 013001, 2008).
69. Habermeier H, Materials Today, 10 (2007).

70. Lee, C.; Wei, X.; Kysar, J. W.; Hone, J. Measurement of the Elastic PropertiesandIntrinsicStrengthofMonolayerGraphene.Science (2008).

71. Hummers, W. S.; Offeman, R. E. Preparation of Graphitic Oxide. J. Am. Chem. Soc. (1958)

72. Pastor, I.R.; Fernandez, G.R.; Rizo, H.V.; Terrones, M.; Gullon, I. M. Towards the Understanding of the Graphene Oxide Structure: How to Control the Formation of Humic- and Fulvic-Like Oxidized Debris. Carbon (2015).

73. Yang, Q.; Pan, X.; Huang, F.; Li, K. Fabrication of High Concentration and Stable Aqueous Suspensions of Graphene Nanosheets by Noncovalent Functionalization with Lignin and Cellulose Derivatives. J. Phys. Chem. C (2010)

74. Hassanpour, A., Ghorbanpour, K. and Tehrani, A. D. Covalent and Non-covalent Modification of Graphene Oxide Through Polymer Grafting, in Advanced 2D Materials, NJ, USA (2016)

75. Mathew D. S. and Juang R. S., "An overview of the structure and magnetism of spinel ferrite nanoparticles and their synthesis in microemulsions," Chemical Engineering Journal, vol. 129, pp. 51-65, (2007).

76. Kumar G. et al. / Materials Research Bulletin 63 (2015).

77. Vasilios, G. et al. Noncovalent Functionalization of Graphene and Graphene Oxide for Energy Materials, Biosensing, Catalytic, and Biomedical Applications. Chemical Reviews (2016)

78. Glumac N., Kear B. H., Skandan G., and Chen Y., "Combustion flame synthesis of nanophase materials," Ed: Google Patents, (1999).

79. Bagwe R. P., Yang C., Hilliard L. R., and Tan W., "Optimization of Dye-Doped Silica Nanoparticles Prepared Using a Reverse Microemulsion Method," Langmuir, vol. 20, pp. 8336-8342, 2004/09/01 (2004).

80. Kim E. H., Lee H. S., Kwak B. K, and Kim B. K., "Synthesis of ferrofluid with magnetic nanoparticles by sonochemical method for MRI contrast agent," Journal of Magnetism and Magnetic Materials, vol. 289, pp. 328-330, (2005).

81. Zhang Y., Yang Z., Yin D., Liu Y., Fei C., Xiong R., et al., "Composition and magnetic properties of cobalt ferrite nano-particles prepared by the co-precipitation method," Journal of Magnetism and Magnetic Materials, vol. 322, pp. 3470-3475, (2010).

82. Xie H., Hu G., Du K., Peng Z., and Cao Y., "An improved continuous co-precipitation method to synthesize LiNi 0.80 Co 0.15 Al 0.05 O 2 cathode material," Journal of Alloys and Compounds, vol. 666, pp. 84-87, (2016)

83. Zhang L., Yu X., Hu H., Li Y., Wu M., Wang Z., Li G., Sun Z., Chen C., Facile synthesis of iron oxides/reduced graphene oxide composites: application for electromagnetic wave absorption at high temperature, Scientific reports, 5 (2015).

84. Fu Y., Wang X., Magnetically separable $ZnFe_2O_4$–graphene catalyst and its high photocatalytic performance under visible light irradiation, Industrial & Engineering Chemistry Research, 50 (2011).

85. http://www.gla.ac.uk/schools/ges/researchandimpact/researchfacilities/isaac/services/scanningelectronmicroscopy/

86. Zhu, F, Wang, Q. et al. 3D nanostructure reconstruction based on the SEM imaging principle, and applications. IOP Publishing Ltd. Nanotechnology, V25, No.18. (2014)

87. Bacon G. E., Neutron Diffraction, Clarendon Press, Oxford (1975).